circuit' reduces spatial specificity of information transfer. However, this leakage may have physiological influence on the circuit behavior such as contrast formation (Krekelberg and Taylor, 1996) or distributed synaptic plasticity (Schuman and Madison, 1994; Hartell, 1996). For this purpose, it is expected that the initial NO concentrations, thereby the spreading areas, are tunable, or graded in response to synaptic inputs. Actually, the NO production rate in ML depended on stimulus frequency and cyclic AMP-dependent protein kinase (Shibuki and Kimura, 1997; Kimura et al., 1998). However, the NMDA receptor mechanism is not suitable to control the graded NO production. Actually, the only variation of NO production through NMDA receptor is pathological, in which prolonged activation of the receptor causes neuronal death (Sattler et al., 1999).

Finally, nNOS immunoreactivities in the cerebellar cortex were found both presynaptically (terminals of PF and basket cell axon called the pinceau) and postsynaptically (dendrites of basket/stellate and granule cells [GC]; Rodrigo et al., 1994). Although it is well known that NMDA receptor is the major trigger of NO production in the postsynaptic sites (Garthwaite et al., 1988; Bredt and Snyder, 1990), mechanism for presynaptic NO production is yet unclear. For example, there is a controversy as to the responsible receptor for NO production in PF terminals (Shibuki and Kimura, 1997; Casado et al., 2000; Hartell et al., 2001). In addition, NO production has not yet been described in the pinceau.

Pharmacological studies revealed that activation of AMPA or type-1 metabotropic glutamate (mGlu-1) receptor also produced NO in the cerebellar slices (Okada, 1992), although contributions of these receptors in total cyclic GMP formation were relatively small (Bredt and Snyder, 1989). These facts and considerations suggested a hypothesis that multiple receptor mechanisms control the efficiency of NO production at specific sites, allowing variation in NO functions. In the present study, we visualized NO production in rat cerebellar cortex by the use of a NO-specific fluorescence indicator dye, diaminofluorescein-2 (DAF-2; Kojima et al., 1998), and found that distinct receptor mechanisms governed NO production in presynaptic sites. AMPA receptor activation produced NO at low concentrations in PF terminals, while synergistic activation of NMDA and mGlu-1 receptors produced NO around Purkinje cell (PC) soma, probably in the pinceau.

EXPERIMENTAL PROCEDURES

Cerebellar slices and culture

Wistar ST rats (7–10 weeks old; Japan SLC, Japan) were decapitated under ether anesthesia, according to RIKEN's guideline of the animal care and use. All efforts were made to minimize the number of animals used and their suffering. Cerebellar vermal slices (usually 300 μm thick and 150 μm in Fig. 2) were prepared with a vibrating slicer (Dosaka EM, Japan) as described (Okada, 2000) in ice-cooled artificial cerebrospinal fluid (ACSF), which contained (mM): NaCl 125, KCl 2.5, $CaCl_2$ 2, $MgCl_2$ 1, NaH_2PO_4 1.25, $NaHCO_3$ 26, glucose 25, and was bubbled with 95% O_2 and 5% CO_2 (pH 7.4). Primary neuronal culture was prepared from E19-20 Wistar ST rat cerebella by the method of Furuya et al. (1998). After digestion with 0.1% trypsin and 0.05% DNAse A at 37 °C, cell suspensions were incubated on a poly-L-ornithine-coated (10 μg/ml) dish at 37 °C for 20 min, then cells not attached to the dish were seeded at 2×10^5 cells/well on poly-L-ornithine-coated (250 μg/ml) plastic sheets (12 mm diameter; Sumilon; Sumitomo Co. Ltd.), and cultured in six-well plates. Ara-C (1 μM) was added to the medium 2–8 days *in vitro* (DIV). Under this condition, about 70% of the cell population was constituted with GCs.

Imaging

Slices or cells on DIV 14–21 were incubated with 10 μM DAF-2 diacetate at 32 °C for 30 min in dark. In some experiments cells were incubated with diaminorhodamine-4M (DAR-4M) AM (10 μM, 30 min) and 1-(4-trimethyl ammoniumphenyl)-6-phenyl-1,3,5-hexatriene-*p*-toluenesulfonate (TMA-DPH; 20 μM; 1 min) at 37 °C (Bronner et al., 1986). To incorporate TMA-DPH into recycling vesicles, cells were stimulated with AMPA for 1 min, washed with ACSF for 60 min, and then stimulated by 90 mM KCl for 2 min at room temperature. Fluorescence representing recycling vesicles appeared in subtraction images (before minus after KCl).

Slices, under constant perfusion with ACSF (1.5 ml/min) maintained at 32 °C using an inline heater (TC344B; Warner, USA), were observed with an upright fluorescence microscope (BX50-WI; Olympus) equipped with a 150 W xenon lamp and an electric shutter (OSP-EXA; Olympus). A platinum weight and a nylon net were used to prevent slice movements. Cultures under constant perfusion with ACSF (0.7 ml/min) at room temperature were observed with an inverted fluorescence microscope (Axiovert S100-25; Zeiss) equipped with a 100 W mercury lamp and an electric shutter (Uniblitz D122; Vincent Associates, USA). Fluorescent images (12 bit, 512×512 pixels) of DAF-2 (exciter 470–490 nm, dichroic mirror 500 nm, emitter >505 nm), DAR-4M (530–560 nm, 570 nm, >605 nm) and TMA-DPH (380–400 nm, 405 nm, 410–460 nm) were acquired with a cooled CCD camera (PXL37; Photometrics, USA). Exposure (50–300 ms) and image acquisition were controlled by an electric stimulator (Master-8; AMPI, Israel). Images were stored in a personal computer (Power Macintosh 9500/200) and analyzed off-line with IPLab software (Scanalytics, USA).

Stimulation

Drugs were applied by switching the medium with a six-way valve (type 50; Rheodyne). Complete exchange of the medium in the chamber took 1 min under the flow rate at 1.5 ml/min, judged from measurement of chloride potential shift. AMPA (1–50 μM, usually 10 μM) and (*S*)-3,5-dihydroxyphenylglycine ((*S*)-DHPG; 100 μM) were applied for 1 and 5 min, respectively. NMDA (30 μM; in some experiments 100 μM) was dissolved in Mg^{2+}-free ACSF containing 10 μM glycine, and applied for 1 min, which was always preceded by application of Mg^{2+}-free ACSF for 15 min. Electrical stimulation (a SEN7203 stimulator and a SS201J isolator; Nihon Kohden, Japan) was given through a tungsten bipolar electrode (WPI; tip resistance 2 MΩ) positioned 150 μm beneath the slice surface. PF presynaptic volleys were recorded (Axopatch 200B; Axon Instruments, USA) with extracellular glass pipettes (5 MΩ) placed on the surface of frontal slices 500 μm apart from the stimulating site (Casado et al., 2000).

Analysis

To find a region of interest (ROI), a subtraction image (response peak minus pre-stimulus average) was made and its pixel intensity histogram was calculated. A ROI was selected among pixels showing changes larger than a half of the maximum change in the histogram. Intensity histogram of an eight-bit image was calculated and pseudocolors were applied (Okada, 2000). Membrane densities affect incorporation of hydrophobic DAF-2 diacetate,

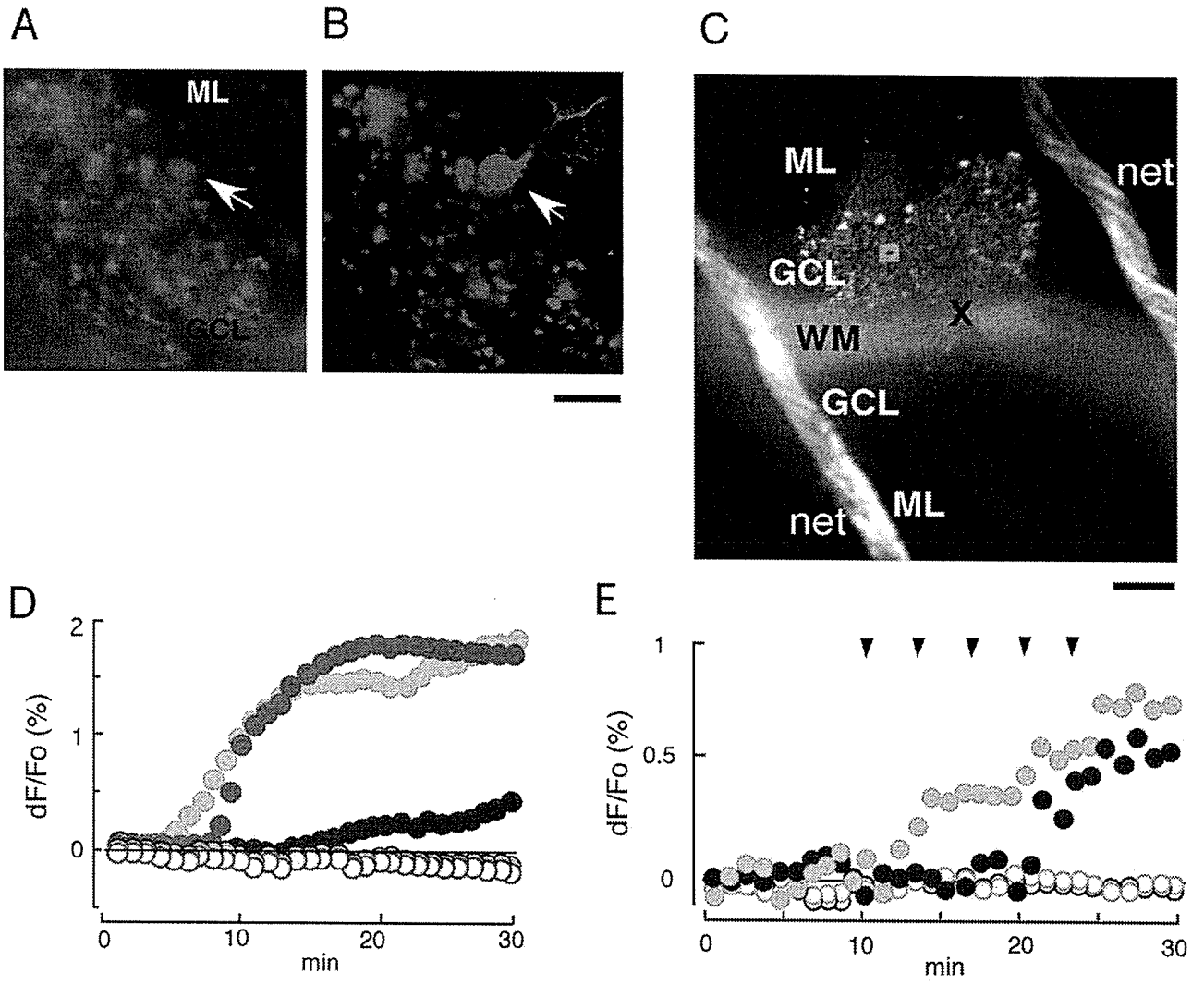

Fig. 1. NO production evoked by electrical stimulation suggests layer-dependent mechanisms. (A–D) Ten trains (0.5 Hz) of 20 biphasic pulses (duration: 0.1 ms; amplitude: ±0.5 V; frequency: 20 Hz) were given to the WM of a sagittal slice every minute. (A) A fluorescence image (×40 objective) before stimulation. Fluorescence in ML was low, while individual GCs are more fluorescent. A PC soma indicated by an arrow was weakly fluorescent. (B) The same site as in A after 30 sets of stimulation (i.e. 30 min after A). Dendrites and soma of a PC indicated by an arrow and GCs are now intensely fluorescent. Scale bar=50 μm. (C) A low magnitude (×5) image of B. Position of stimulation is indicated by a X. The nylon net preventing movement of slice is seen (net). Scale bar=100 μm. (D) Fluorescence changes in ROIs shown by squares in C were measured and normalized in the initial intensity (dF/Fo). A representative experiment from six similar experiments is shown by closed symbols. Green, GC; red, PC soma; blue, ML. Similar experiments were done in the presence of 10 μM L-NAME (open symbols). A representative experiment from three similar experiments is shown. (E) ML of a frontal slice was stimulated with five trains (0.5 Hz) of 50 biphasic pulses (duration: 1 ms; amplitude: ±30 V; frequency: 50 Hz) at time points indicated by arrowheads. A representative experiment from three similar experiments is shown by closed symbols. Green, GCL; blue, ML. Similar experiments were done in the presence of 10 μM L-NAME (open symbols). A representative experiment from three similar experiments is shown.

thus intracellular DAF-2 concentrations. Actually, GC layer (GCL) showing granular patterns of intense fluorescence was easily discriminated from ML where almost even staining was observed. Comparison of the fluorescence increase between different layers therefore requires normalization by the initial fluorescence intensity (dF/Fo), while fluorescence time courses within one ROI can be expressed by fluorescence increase (dF).

Materials and other methods

DAF-2 diacetate (Kojima et al., 1998) and DAR-4M AM (Kojima et al., 2001) were synthesized as reported, or supplied from Daiichi Pure Chemicals Co. Ltd. (Japan). NMDA (Nakalai Tesque, Japan), (*S*)-AMPA, (*S*)-DHPG, 7-(hydroxyimino)-cyclo propa-[b]-chromen-1a-carboxylate ethyl ester (CPCCOEt), 6-cyano-7-nitro quinoxaline-2,3-dione disodium salt (CNQX), D-2-amino-5-phosphonovaleric acid (D-AP5), N^{ω}-nitro-L-arginine methyl ester (L-NAME; Tocris Cookson, UK), *N*-(dithiocarboxy)-sarcosine (DTCS; Dojindo, Japan), ω-conotoxin-GIVA, ω-agatoxin-TK, nifedipine (Alamone Laboratory, Israel), TMA-DPH (Molecular Probe, USA) and tetrodotoxin (TTX; Seikagaku Kougyo, Japan) were purchased. Cyclic GMP was measured using an enzyme-linked immuno assay kit (Amersham Pharmacia, UK) as reported (Miyata et al., 1999).

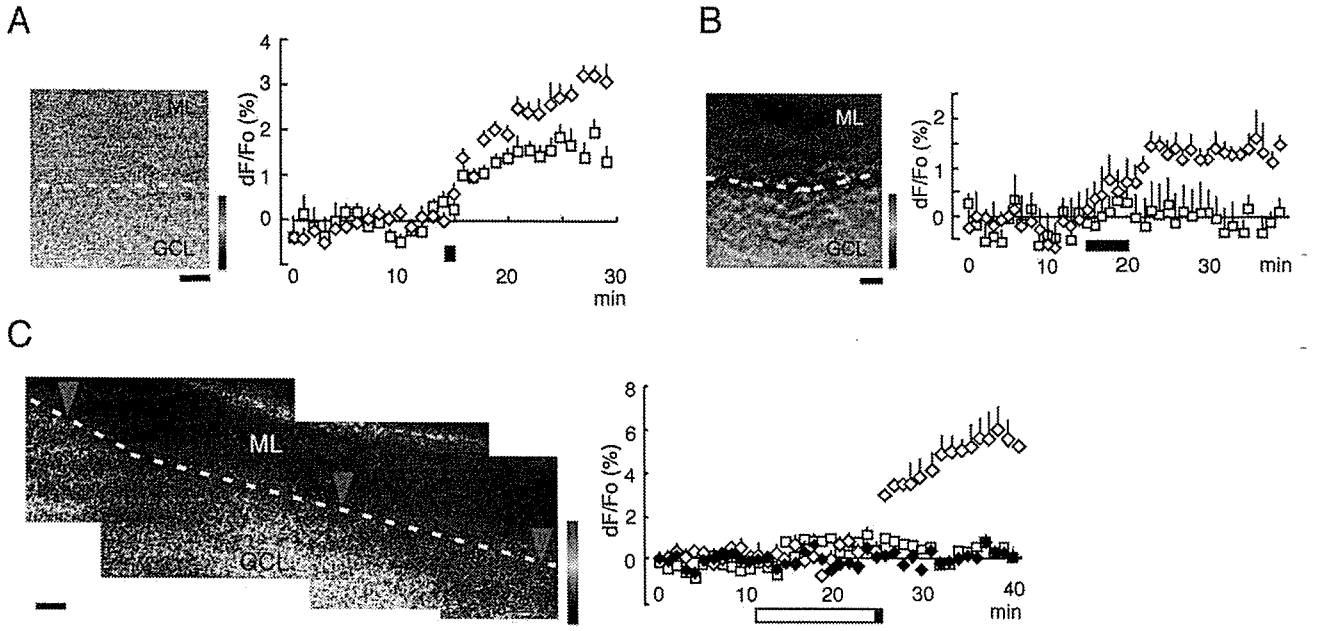

Fig. 2. Differential NO production by type-specific glutamate receptor agonists. (A, B) A receptor type-specific agonist was applied to thin (150 μm thick) horizontal slices. (Left) A subtraction image (20 min after stimulation−before, ×20 objective). Broken lines indicate PCL. Scale bar=20 μm. (Right) The time course of average dF/Fo in five ROIs (squares, ML; diamonds, GCL) are shown. Vertical bars are S.E.M. Horizontal bars represents application of 10 μM AMPA (A) and 100 μM (S)-DHPG (B). (C, Left) Fluorescence images (×10) were taken in adjacent regions in the lobule VI before and after 30 μM NMDA application. Images were aligned and subtraction images were calculated, equal pseudocolors were applied to corresponding loci, and merged. Regions with intense fluorescence increase appeared discontinuously as indicated by arrowheads. (Right) Averages of dF/Fo in five ROIs are shown over time. Open and closed bars indicate application of Mg-free ACSF and NMDA, respectively. Open diamonds, GCL with increase; closed diamonds, GCL without increase; squares, ML. Scale bar=100 μm.

RESULTS

Entire picture of NO production in the cerebellar cortex

Fig. 1A shows an example of DAF-2 fluorescence in a parasagittal slice before stimulation. Weak fluorescence was found uniformly in neurons, consistent with the amphipathic nature of the DAF-2 (DAR-4M as well) molecule. Incorporation in glia was not evident. Perfusion with ACSF alone did not alter the fluorescence for at least 1 h. To know the entire sites of NO production in the cerebellar cortex, electrical stimulation was given repeatedly to the white matter (WM) of parasagittal slices (n=6). Fig. 1B and C shows that GCs, PCs and ML were intensely fluorescent. Although PCs do not express nNOS (Crepel et al., 1994), a whole PC was fluorescent, indicating that the PC received NO derived from surrounding sources, consistent with our previous observations (Hartell et al., 2001). As seen in Fig. 1C, a restricted region of a folium responded, showing that our stimulation activated specific neural circuits. Fig. 1D (closed symbols) shows an example of experiments (n=3) where a NOS inhibitor, L-NAME at 10 μM, blocked the increase, confirming the fluorescence change was due to NO production. We confirmed the blockade by L-NAME of the fluorescence change for all types of electrical or agonist stimulation in this study (see Discussion).

Fig. 1D also shows that onset and magnitude of fluorescence increase differed in each layer: fluorescence increase in ML was much lower and required more numbers of stimulation than the other layers. Although the onset delays somewhat differed among experiments, this tendency was constantly observed. Such a delayed onset may reflect attenuation of conduction between distant sites (from WM to ML), or it may reflect the fact that most of PFs are cut in parasagittal slices. Alternatively, single stimulation may produce different concentrations of NO in each layer. To clarify this issue, ML of frontal slices, where PFs are preserved, was stimulated repeatedly. Since the stimulation parameters used in sagittal slices did not alter fluorescence in GCs of frontal slices, stronger stimulation parameters were applied to activate GCs retrogradely. This stronger stimulation successfully increased fluorescence in both layers. As shown in Fig. 1E, the fluorescence increase in ML, which was inhibited by L-NAME, also required more numbers of stimulation than in GCL (n=3): GCL and ML required one to two and three to four trains of stimulation, respectively. Thus, the delayed onset was independent of stimulation sites or direction of slice sectioning. These results are consistent with the idea that NO production rate in ML is lower than in the other area.

Localization of NO production by specific receptor activation

Results shown in Fig. 1 were consistent with the hypothesis that each layer employs different NO producing mechanisms. Pharmacological stimulation of each receptor further supported this idea. Application of 1–50 μM AMPA increased fluorescence in ML of horizontal (n=4; Fig. 2A), parasagittal (n=3; see Fig. 6A) and frontal slices (n=3; not shown). In contrast, a specific agonist of mGlu-1 receptor,

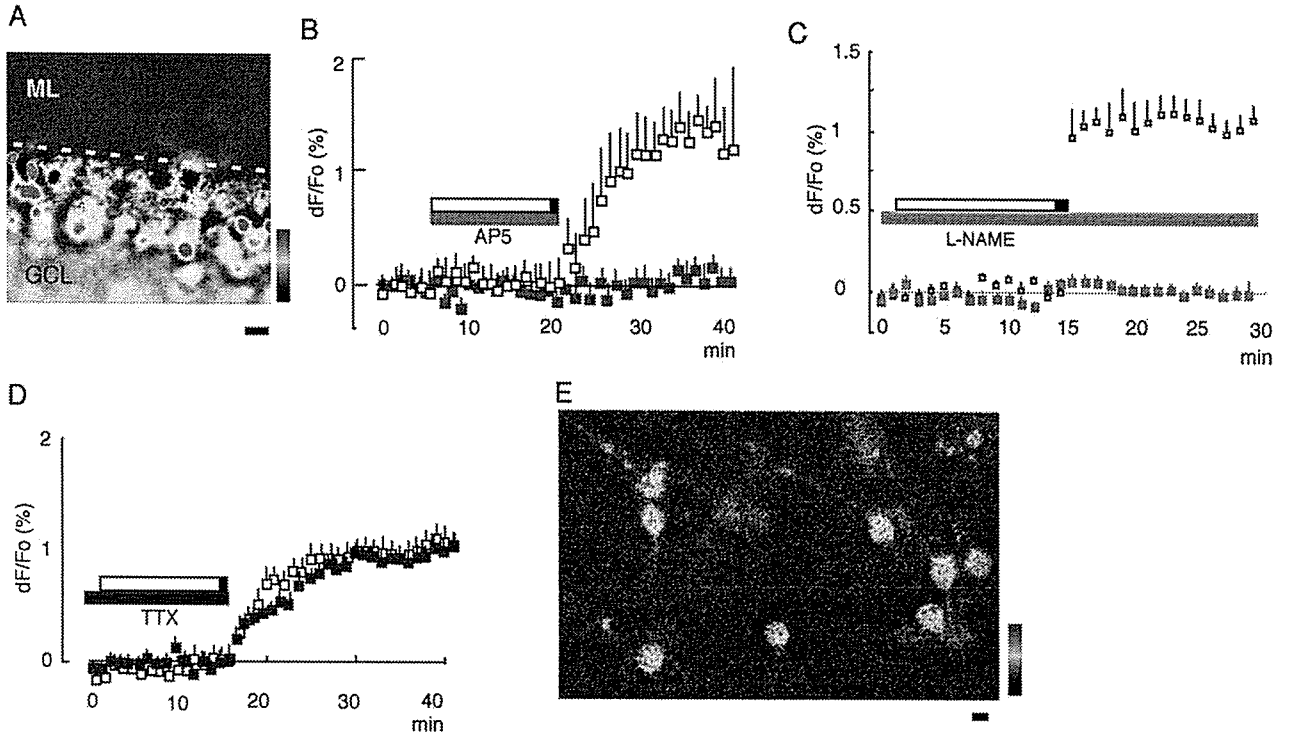

Fig. 3. NMDA receptor-dependent NO production. (A) A subtraction image (×40) showing response of a parasagittal slice to 30 μM NMDA. Broken line indicates PCL. Note that response was seen only in GCL. (B–D) Fluorescence increases evoked by NMDA (open symbols) in GCL of parasagittal slices were inhibited by 50 μM D-AP5 (red symbols; four ROIs from three slices; B) and 10 μM L-NAME (green symbols; 10 ROIs from five slices; C), but not by 1 μM TTX (blue symbols; 10 ROIs from three slices; D). Antagonists, Mg-free ACSF and NMDA were applied during periods indicated by colored, open and black bars, respectively. Averages and S.E.M. (vertical bars) of dF/Fo are shown. (E) A subtraction image (×40 objective) depicting NMDA-dependent fluorescence increase in soma of GCs in culture on DIV 15. Scale bars in A and E=20 μm and 10 μm, respectively.

(*S*)-DHPG (100 μM; horizontal slices, n=4, Fig. 2B; parasagittal slices, n=5, not shown), or NMDA (30 μM; horizontal slices, n=3, Fig. 2C; parasagittal, n=5, see Fig. 3A; frontal, n=3, not shown) did not alter it. These results depicted the major contribution of AMPA receptor to NO production in ML, while contributions of NMDA and mGlu-1 receptors were under the detection level.

In contrast, DAF-2T fluorescence in GCL was increased by all of the agonists used. AMPA (Fig. 2A) or (*S*)-DHPG (Fig. 2B) increased fluorescence uniformly in the entire GCL. However, NMDA application resulted in fluorescence increase in discontinuous areas in GCL of thin (150 μm thick) horizontal slices (folium VI, n=3, Fig. 2C). We could not detect such a discontinuous pattern in frontal and sagittal slices.

NMDA receptor mechanisms

NMDA application to sagittal slices specifically increased fluorescence in GCL (Fig. 3A), which was blocked by D-AP5 (n=3, Fig. 3B) or L-NAME (n=5, Fig. 3C), indicating that NMDA receptor-dependent NOS activation takes place in GCL. A close linkage between NMDA receptor-mediated calcium influx and nNOS activation (Christopherson et al., 1999) suggests that NMDA triggers NO production without conduction of depolarization in the absence of extracellular Mg^{2+} ions. This idea was confirmed by experiments shown in Fig. 3D, where TTX did not affect NMDA-dependent NO production in GCL (n=3). When NMDA was applied to GCs in dissociated culture, fluorescence was increased predominantly in the soma, and the proximal neurites to a less extent, but not in the fine, distal neurites (n=5, Fig. 3E), suggesting postsynaptic localization of the mechanism.

AMPA receptor mechanisms

When frontal slices were received electric stimulation (parameters identical to that used in Fig. 1E) in ML, an AMPA receptor antagonist, CNQX, blocked the fluorescence increase in ML (n=4, Fig. 4), while a NMDA receptor antagonist, D-AP5, had no significant effect (n=4, Fig. 4). These results were consistent with results shown in Fig. 2, confirming the major contribution of AMPA receptors in NO production in ML. Fluorescence increases in ML and GCL evoked by bath-applied AMPA were also inhibited by CNQX (n=4, Fig. 5A), or L-NAME (n=4, Fig. 5B), but not by D-AP5 (n=2, Fig. 5A). These results confirmed that AMPA receptor, but not NMDA receptor, triggered NOS activation. In contrast to NMDA, TTX reduced the AMPA-dependent NO production in both ML and GCL (n=6, Fig. 5C), suggesting that AMPA receptor and NOS are indirectly linked through conduction of depolarization. AMPA also increased fluorescence of GCs in culture (Fig. 5D), which was similarly inhibited by CNQX (n=4), L-NAME (n=4) or TTX (n=3) (data not shown). In both slices (ML and GCL) and culture, a blocker of N-type calcium

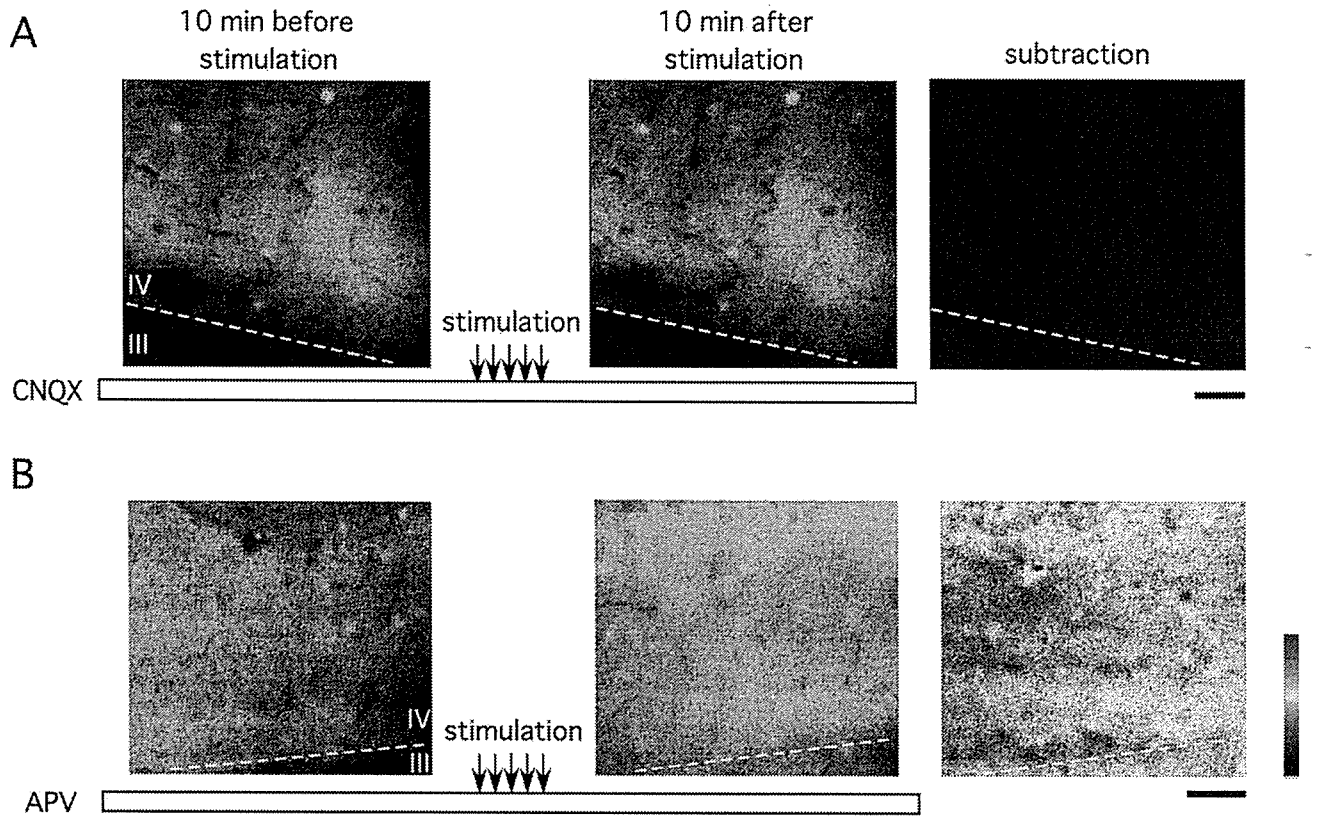

Fig. 4. AMPA receptor is responsible for NO production in ML. ML of a frontal slice was electrically stimulated (50 biphasic pulses with 1 ms of duration and ±30 V of amplitude at 50 Hz, five trains every 2 s, shown by arrows). CNQX (50 μM) abolished fluorescence change in ML (A), while D-AP5 (50 μM) did not suppress it (B). (Left and Center) Raw fluorescence images of ML before and after stimulation are shown in pseudocolors. (Right) A peristimulus subtraction image. Broken lines indicate the border of folia III and IV. Scale bars=20 μm.

channel, ω-conotoxin-GIVA (1 μM, 10 min, n=3 for each, Fig. 5E), or P/Q-type calcium channel, ω-agatoxin-TK (0.1 μM, 10 min, n=3 for each, Fig. 5F), abolished AMPA-dependent fluorescence increase, whereas the L-type channel blocker, nifedipine had no effect (10 μM, 10 min, n=3 for each, Fig. 5G). These results are consistent with the previous reports (Okada, 1992; Shibuki and Kimura, 1997) and demonstrated that calcium influx in compartments linked to N- and P/Q-type calcium channels activate NOS after conduction of depolarization triggered by AMPA receptor activation.

Although AMPA produced NO in the entire ML relatively uniformly in horizontal (Fig. 2A) and frontal slices, the response was not uniform in parasagittal slices (Fig. 6A) where only a small portion of PFs is connected with the originating GCs. As shown in Fig. 6A, regions with larger increases were recognized as fluorescent patches. Line-scan analysis of such a patch (Fig. 6B) showed that NO was generated from small sources, because the increase started from single pixels. These single fluorescent pixels were then merged to shape the fluorescence patch (about 5 μm of radius).

Immunohistochemical studies (Rodrigo et al., 1994) showed that PF terminals and interneurons are possible NO sources in ML. To distinguish these possibilities we noticed difference in their size. A water-soluble NO scavenger, Fe-DTCS (Fujii et al., 1998), that traps extracellular NO, was used to highlight single components of the source by scavenging intercellularly spreading NO. If PF terminals are the source, the patches should disappear in the presence of the scavenger, because single components (=terminal) are very small (<1 μm) compared with the patch (10 μm). Alternatively, if interneurons are the source, NO spreading inside the cell will not be wiped out by the scavenger; therefore, as a result interneuron should be highlighted. Because the diameter of the single components (=interneuron soma) is similar to that of the patch, they should not disappear, but even be highlighted, in the presence of scavenger. Results showed that Fe-DTCS eliminated the patches (n=3, Fig. 6C), suggesting that intercellular diffusion of NO from PF terminals shaped the patch. NO release from PF terminals was directly detected GCs in culture, where AMPA increased DAF-2 fluorescence in fine fibers, as well as in soma (Fig. 6D). To confirm NO production at PF terminals, recognized as axonal varicosities, GCs in culture were doubly stained with DAR-4M, another NO-specific indicator with red fluorescence (Kojima et al., 2001), and TMA-DPH, an activity-dependent endocytosis marker with blue fluorescence (Bronner et al., 1986). This dual staining enabled simultaneous observation of NO production and activity-dependent endocytosis that occurs predominantly in presynaptic terminals. The result indicated colocalization of endocyto-

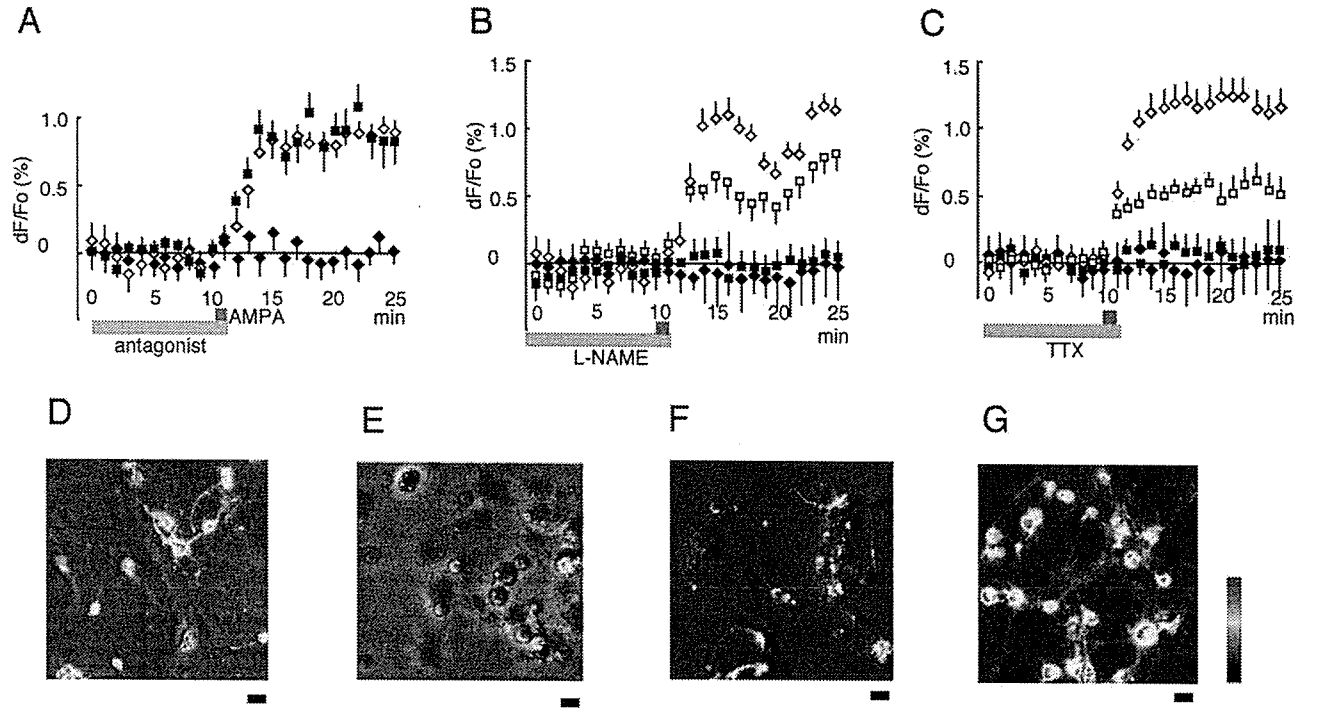

Fig. 5. AMPA receptor-dependent NO production. (A) Fluorescence increases evoked by AMPA (open diamonds, five ROIs from five slices) in ML of parasagittal slices were inhibited by CNQX (closed diamonds, five ROIs from four slices), but not by AP5 (closed squares, n=8 ROIs from two slices). Antagonists were applied during periods indicated by a blue bar, while a red bar indicates AMPA application. Averages and S.E.M. (vertical bars) of dF/Fo are shown. (B) Fluorescence increases evoked by AMPA in ML (open squares, four ROIs from four slices) and in GCL (open diamonds, two ROIs from two slices) of parasagittal slices were inhibited by L-NAME (ML, closed squares, four ROIs from four slices; GCL, closed diamonds, three ROIs from three slices). (C) Fluorescence increases evoked by 10 μM AMPA in ML (open squares, five ROIs from three slices) and GCL (open diamonds, two ROIs from two slices) of parasagittal slices were inhibited by 1 μM TTX (ML, closed squares, seven ROIs from six slices; GCL, closed diamonds, three ROIs from two slices). (D–G) Subtraction images (×40 objective, after−before 6 μM AMPA) of GCs in culture on DIV15. AMPA response in GC culture (D) was blocked by ω-conotoxin GVIA (1 μM, 10 min, E), or ω-agatoxin TK (0.1 μM, 10 min, F), but not by nifedipine (100 μM, 10 min, G). Scale bars=10 μm.

sis and NO production in cluster on fine fibers (n=4, Fig. 6E). Thus, Fig. 6C–E indicates that AMPA receptor activation produced NO in PF terminals.

Synergistic effect of NMDA and mGlu-1 receptors

NMDA at a higher concentration (100 μM) sometimes increased fluorescence in PC layer (PCL; n=3 of 9 slices). We therefore searched for the condition that could reproducibly evoke NO production in PCL, and found that electrical stimulation of WM at 50 Hz consistently increased fluorescence in PCL (n=6, Fig. 7Aa and Ac), while similar stimulation at 10 Hz did not (n=6, Fig. 7Ab and Ac). TTX (n=2, Fig. 7B) or L-NAME (n=4, not shown) blocked the fluorescence increase in PC. The frequency dependency suggested involvement of mGluR activation (Batchelor and Garthwaite, 1997). Actually, the 50 Hz-stimulation in the presence of 100 μM CPCCOEt, a selective blocker of mGlu-1 receptor (n=3, Fig. 7C), or D-AP5 (n=3, Fig. 7D) failed to increase fluorescence. As shown in Fig. 2B, (*S*)-DHPG alone increased fluorescence in GCL, but not in PCL. However, the 10 Hz-stimulation increased fluorescence in PCL in the presence of 100 μM (*S*)-DHPG (n=6, Fig. 7E). These results suggested that combined activation of NMDA and mGlu-1 receptors is necessary and sufficient for NO production in PCL. To show this critically, we applied 30 μM NMDA after a 10 min-application of 100 μM (S)-DHPG, and observed NO production in PCL (n=3, Fig. 7F).

PC soma does not express nNOS, but is surrounded by the axon terminal plexus of basket cell, the pinceau. Basket cells express NR-1 (ζ) and 2D (ε4) subunits of NMDA receptor (Watanabe et al., 1994; Petralia et al., 1994a,b), as well as mGlu-1 receptor (Baude et al., 1993), nNOS (Rodrigo et al., 1994) and PSD-95 (Hunt et al., 1996). Therefore, the fluorescence increase in PCL likely represents NO production in the pinceau triggered by synergistic activation of NMDA and mGlu-1 receptors. Co-application of (*S*)-DHPG and NMDA also synergistically increased cyclic GMP content in cerebellar slices. As shown in Fig. 7G, cyclic GMP level achieved by (*S*)-DHPG+NMDA was significantly higher than the simple summation of that achieved by each agonist alone (P<0.01, t-test, n=5). Either CPCCOEt (P<0.01) or D-AP5 (P<0.05) blocked the synergistic increase in cyclic GMP. These results showed that coactivation of NMDA and mGlu-1 receptors triggers synergistic NO production and increases cyclic GMP levels in cerebellar slices. Although the site of the synergistic cyclic GMP increase is not clear, this is likely to be triggered by synergistic activation of NOS in the pinceau.

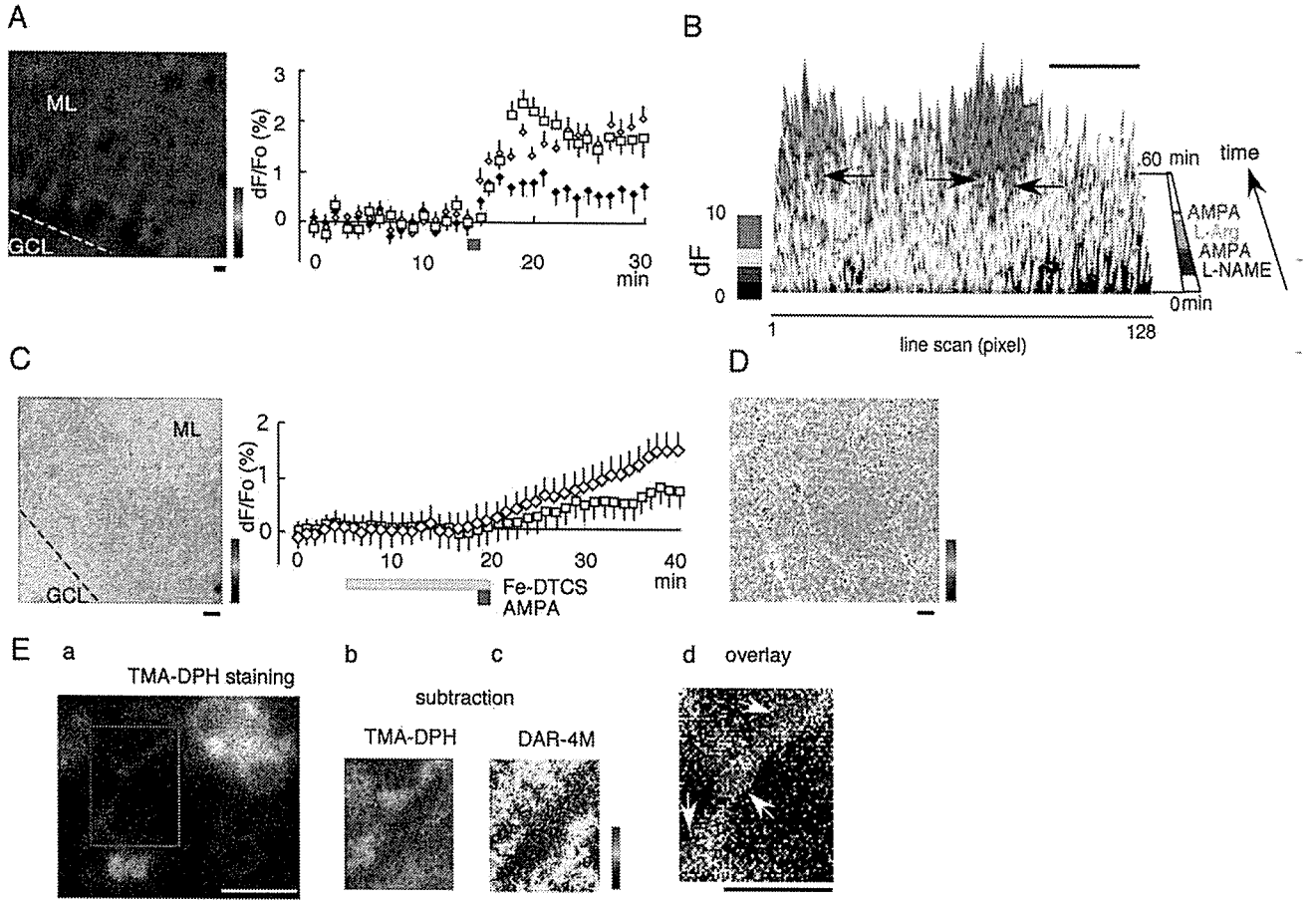

Fig. 6. AMPA receptor activation produces NO in PF terminals. (A, Left) A subtraction image (×40) showing response to AMPA of the parasagittal slice. Patches expressing larger fluorescent increase are seen in ML. Scale bar=10 μm. (Right) Averages and S.E.M. (vertical bars) of dF/Fo in several ROIs of three slices are shown. The red bar indicates AMPA application. Open diamonds: within patches in ML (five ROIs), closed diamonds: between patches in ML (eight ROIs), open squares: GCL (three ROIs). (B) Line-scan analysis of the intense fluorescent patch in ML. Images were taken every minute and a series of subtraction images from the initial picture were made. A linear ROI of 128-pixel long crossing a patch (horizontal axis) was selected and fluorescence change over time is indicated by pseudocolors. Scale bar=10 μm. Time course is expressed from the front to the back of the figure. Drugs were applied as indicated in the right. AMPA in the presence of L-NAME had no effect. L-Arginine (10 mM) was applied then the second challenge by AMPA increased fluorescence. The increase started from single pixels (arrows) and spread laterally. (C, Left) A subtraction image (×40 objective) showing that 100 μM Fe-DTCS (10 min) caused weak, uniform response to 10 μM AMPA in ML of a parasagittal slice (compare with Fig. 6A). The broken line indicates PCL. Scale bar=10 μm. (Right) Average and S.E.M. of dF/Fo in ML (open squares, n=6 ROI from three slices) and GCL (open diamonds, n=6 ROI from three slices) in the presence of Fe-DTCS. (D) A subtraction image (×10 objective) showing the response to 10 μM AMPA of GC culture in soma and fibers. Hot spots on fine fibers originated from the cell (below, left) are observed as red spots. Scale bar=10 μm. (E) Fluorescence increases in TMA-DPH (b) and DAR-4M (c) in a ROI (a) were binarized with a threshold at mean+2 S.D. TMA-DPH spots (green) and DAR-4M spots (red) were expressed as color dots and merged. This overlay figure (d) shows three clusters where both fluorescence dots are colocalized on a fiber (arrows), which are indicative of presynaptic production of NO. To emphasize changes on the fibers, only fluorescence on fibers were shown. Scale bars=10 μm.

DISCUSSION

The present study demonstrated that presynaptic NOS immuno-positive sites in the cerebellar cortex (Rodrigo et al., 1994), actually served as active NO sources. NO production in PF terminals depended exclusively on AMPA receptors. The AMPA receptor-dependent mechanism involves TTX-sensitive sodium channels and voltage-gated calcium channels, and produces low concentrations of NO presynaptically. This contrasts the NMDA receptor-dependent postsynaptic NO production, which releases NO via calcium entry through the receptor-coupled channel. In addition, we found that synergistic activation of NMDA and mGlu-1 receptors triggered NO production in the pinceau. Together, these findings suggest that multiple gating receptor mechanisms govern NO production in specific neurons.

NO detection with DAF-2 fluorometry

DAF-2 diacetate is a membrane permeable, non-fluorescent compound. It is intracellularly converted to DAF-2, which in turn reacts with NO to produce a stable triazole compound, DAF-2T. This conversion is associated with a 250-fold increase in fluorescence, enabling sensitive (up to 5 nM *in vitro*) detection of NO (Kojima et al., 1998; Räthel et al., 2003). In tissues, however, the sensitivity may be reduced because light scattering and absorption interfere with fluorescence

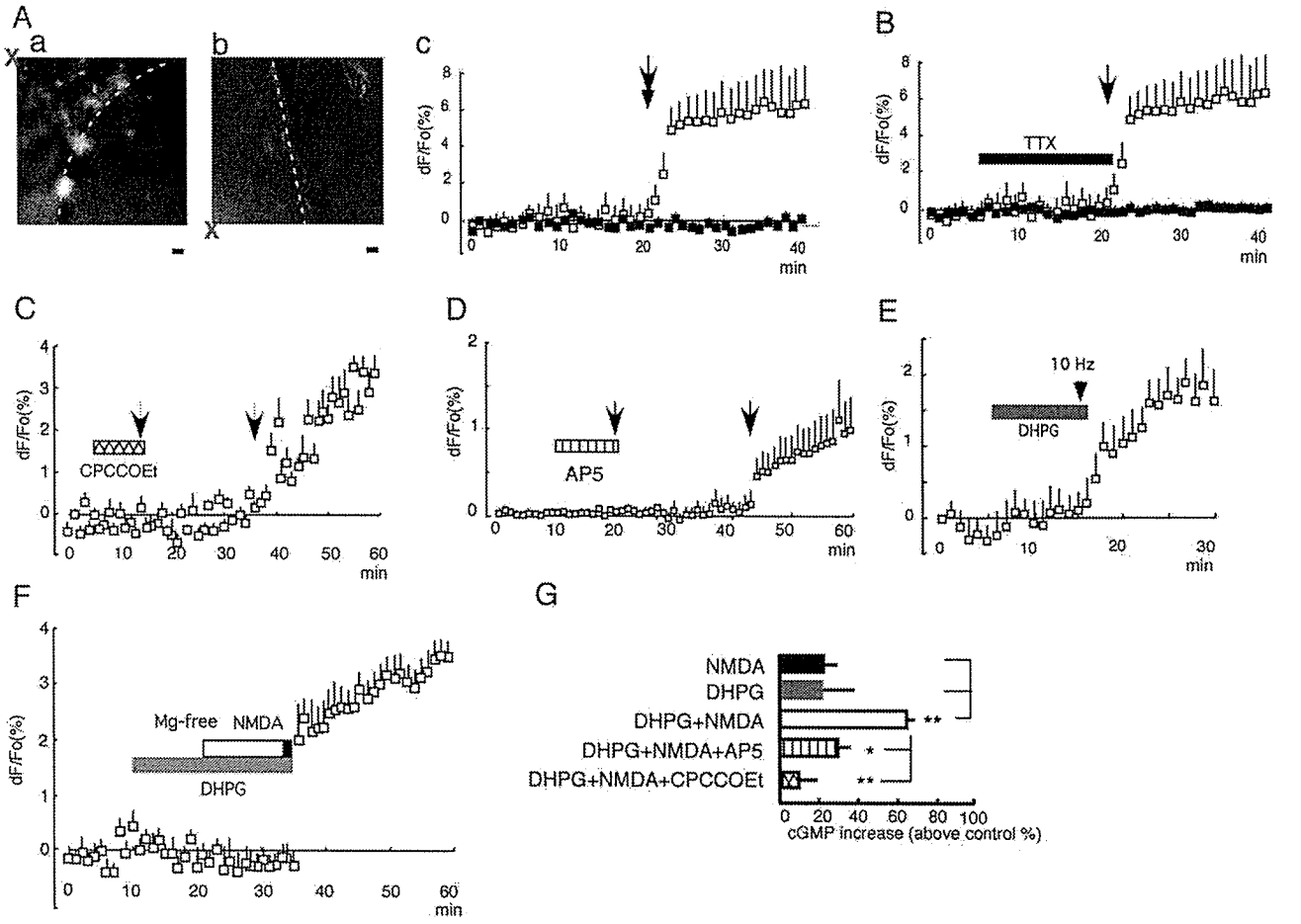

Fig. 7. Synergistic activation of NMDA and mGlu-1 receptors produces NO in PCL. (A) Subtraction images (×40 objective, after−before stimulation, parasagittal slices) showing that fluorescence spots appeared in PC soma after electric stimulation at 50 Hz (2 s, 30 V, Aa), but not at 10 Hz (Ab). The stimulation electrode was placed in WM (marked by X). (Ac) Average and S.E.M. of dF/Fo in a PC soma. The arrow (50 Hz) or arrowhead (10 Hz) indicates stimulation. Open squares: 50 Hz (six ROIs from six slices), closed squares: 10 Hz (six ROIs from six slices). (B) Fluorescence was not increased by 50 Hz stimulation (arrow) in the presence of 1 μM TTX (closed bar). Averages and S.E.M. of dF/Fo in four ROIs from three slices are shown. Open squares: without TTX, the same data as in Ac. Closed squares: with TTX. (C) Stimulation at 50 Hz (arrows) did not increase fluorescence in PC soma in the presence of 30 μM CPCCOEt (hatched bar). Averages and S.E.M. of dF/Fo in five ROIs from three slices are shown. (D) Stimulation at 50 Hz (arrows) did not increase fluorescence in PC soma in the presence of 50 μM D-AP5 (hatched bar). Averages and S.E.M. of dF/Fo in five ROIs from three slices are shown. (E) Stimulation at 10 Hz (arrowheads) increased fluorescence in PC soma in the presence of 100 μM (*S*)-DHPG (shaded bar). Averages and S.E.M. of dF/Fo in 15 ROIs from six slices are shown. (F) Soma response was evoked by 30 μM NMDA (closed bar, open bar indicates Mg-free ACSF) primed by 100 μM (*S*)-DHPG (shaded bar). Averages and S.E.M. of dF/Fo in nine ROIs from three slices are shown. (G) Accumulation of cyclic GMP measured by enzyme-linked immunoassay of slice extract. Slices were incubated with 0.1 mM 3-isobutyl-1-methylxanthine from 5 min prior to addition of agonists. ** $P<0.01$, * $P<0.05$. Averages and S.E.M. of five slices are shown.

detection. Nitrite, nitrate, superoxide, hydrogen peroxide and divalent cations such as calcium and magnesium do not affect DAF-2 fluorescence (Kojima et al., 1998; Suzuki et al., 2002). Although dehydroascorbic acid and ascorbic acid increased DAF-2 fluorescence, the reaction requires these compounds at concentrations >mM (Zhang et al., 2002). Thus, NO specifically converts DAF-2 into DAF-2T in living tissues.

It was reported that oxidation of DAF-2 by peroxynitrite (Jourd'heuil, 2002) or intense light (Broillet et al., 2001) also increased its fluorescence. However, peroxynitrite generation in cells requires NO production, and intense light increases DAF-2 fluorescence only in the presence of NO. Therefore, although these reactions might enhance fluorescence when NO is produced, they do not disguise the fact of NO production. We constantly confirmed NOS-dependent NO production using a NOS inhibitor.

It is, however, noteworthy that quantitative measurements of NO concentrations within tissues, such as direct comparison of NO concentrations between areas, are beyond the ability of DAF-2 fluorometry, because conversion of DAF-2 into DAF-2T is not accompanied with spectral shift, preventing calibration by 2-wavelengths measurement. We concluded that the unit NO release was much less in ML, based on the observation that a detectable fluorescence increase in ML required more numbers of stimuli than other areas (Fig. 1).

DAF-2T fluorescence depicts diffusion-based spread of NO around active NO sources (Fig. 6B). Distributions of DAF-2 and DAF-2T were uniform within a cell (Fig. 1). NO

spreading area would merge together where weak NO sources are present at high density (Lancaster, 1994). This diffusibility of NO, together with light scattering by slice thickness, lowers contrast of our fluorescence images, preventing precise identification of individual active NO sources. However, the use of dispersed cells or an extracellular NO scavenger reduced this ambiguity. Furthermore, differential fluorescence intensity due to membrane density difference among layers enabled discrimination of each layers.

Reaction of DAF-2 with NO occurs within several seconds (Kojima et al., 1998). Since DAF-2T is stable in cells (Kojima et al., 1998), growth of DAF-2T fluorescence over time provides a cumulative map of NO generation in the tissue. Agonist permeation across slice thickness may cause continuous growth of fluorescence after cessation of agonist application observed in some figures such as Fig. 6C.

NMDA-dependent NO production

The NMDA receptor-coupled mechanism activates nNOS close to the receptor. Although it was reported that NO production evoked by 300 μM NMDA in the presence of Mg^{2+} ions was TTX-sensitive (Southam et al., 1991), it was TTX-insensitive in the absence of Mg^{2+} ions in our hands. Since we used lower concentrations of NMDA (30 μM), it is suggested that the effects of NMDA are dose-dependent; both TTX-sensitive and -insensitive components would be activated at higher concentration, while lower concentrations of NMDA activate only postsynaptic NO production.

The discontinuous patterning of NO production was also found by histochemical experiments of nNOS, NADPH-diaphorase (Hawkes and Turner, 1994; Yan et al., 1993) and cGMP (DeVente et al., 1990). This sagittal band is developed in a manner dependent on the pattern of the mossy fiber inputs (Oberdick et al., 1998). Since NMDA activates nNOS in the postsynaptic density complex, it is likely that the banding pattern represents a partial fraction of nNOS linked to NMDA receptors in postsynaptic sites. In contrast, observation of uniform NO production throughout GCL suggests a possibility that a population of nNOS localized extrasynaptically is linked to AMPA and mGlu-1 receptors.

NO production in ML

NO production in ML increases cyclic GMP levels in PCs (Hartell et al., 2001), which is critical for long-term depression of PF synapses (Shibuki and Okada, 1991; Lev-Ram et al., 1995). It has been reported that PF activities produced NO in ML (Shibuki and Kimura, 1997; Casado et al., 2000; Hartell et al., 2001), although responsible receptors were controversial. The present study demonstrated that AMPA receptor is the major trigger of NO production in ML, which causes depolarization of GC and calcium influx in PF terminals through opening voltage-gated calcium channels. These results are consistent with our previous observation (Hartell et al., 2001).

In contrast to NMDA-dependent mechanism, AMPA receptor-dependent NO production was entirely sensitive to TTX and dependent on high-threshold calcium channels, implying the indirect coupling of AMPA receptor with remote nNOS through conduction of depolarization. Molecular organization of such an indirect coupling (for example, relative distance between the receptor and nNOS, or how calcium channels and nNOS are coupled) remains to be investigated; however, our observations indicate that such a "remote" mechanism is important in axonal production of NO, which works as a neuronal output. This contrasts the postsynaptic NO production that functions as one of the elements of dendritic computation. Thus, AMPA- and NMDA-dependent mechanisms generate NO carrying distinct computational information (Garthwaite, 1991).

The present study indicated that the gate-receptors regulate initial NO concentrations. Close linkage between NMDA receptor and nNOS allows NO production at a near-maximal rate, while the indirect activation gated by AMPA receptor does not. Theoretical works (Wood and Garthwaite, 1994; Lancaster, 1994) estimated that NO generated by NMDA receptor-dependent full activation of nNOS spreads over 100 μm, which contains about 5×10^4 synapses in ML, judged from the reported density of spines (Ito, 1984). In contrast, brighter patches representing intercellular diffusion of NO originated from PF terminals (Fig. 6) had a radius of 5 μm and may contain 420 PC spines. Since the number of the NO-generating PFs present in a patch is not necessarily 1, NO diffusion distance from a single source may be less than 5 μm, which is much less than expected from NMDA receptor-dependent mechanism. Since above estimation depends on the detection limit of DAF-2T fluorescence, precise estimation of NO diffusion in tissue requires further efforts. Nevertheless, we suggest that recruitment of the AMPA receptor-dependent mechanism limits the number of the affected synapses. Low initial concentrations of NO may delimit regions that undergo plastic changes in synaptic transmission. Modulation of input specificity of synaptic function by a diffusible messenger sounds paradoxical; however, it might be important for error-tolerant processing by neuronal circuit.

Synergistic production of NO in the pinceau

NO production in the pinceau was observed only after specific pharmacological or electrical stimuli: coactivation of mGlu-1 receptor with NMDA receptor, but not AMPA receptor (Okada, 1992), or electrical stimulation at 50 Hz, but not at 10 Hz. It is thus suggested that specific neuronal inputs activate nNOS in the pinceau through a TTX-sensitive "remote" mechanism. Since mGlu-1 receptor is always found in postsynaptic sites (Baude et al., 1993), nNOS activation in the pinceau may involve modification of NMDA receptor current or intracellular calcium dynamics by mGlu-1 receptor (Skeberdis et al., 2001). Basket cells regulate excitability of PCs through strong inhibitory transmission, and our observation of NO production in the pinceau indicates that NO is released together with GABA.

Therefore, it is possible that NO from the pinceau modulates GABA function through GABA-A receptor phosphorylation or GABA transporter inhibition (Robello et al., 1996; Shen et al., 1997). As another possibility, NO from this site may affect gene expression in PC (Peunova and Enikolopov, 1993; Gudi et al., 2000).

Acknowledgements—We thank Dr. Ryoji Yano (Riken) for partial support and Dr Kaoru Inokuchi (MITILS) for critical comments on the manuscript. This work was partially supported by a grant from Toyota Institute of Physical and Chemical Research.

REFERENCES

Batchelor AM, Garthwaite J (1997) Frequency detection and temporally dispersed synaptic signal association through a metabotropic glutamate receptor pathway. Nature 385:74–77.

Baude A, Nusser Z, Roberts JDB, Mulvihill E, McIlhinney RAJ, Somogyi P (1993) The metabotropic glutamate receptor (mGluR1) is concentrated at perisynaptic membrane of neuronal subpopulations as detected by immunogold reaction. Neuron 11:771–787.

Boehme GA, Bon C, Stutzman J-M, Doble A, Blanchard J-C (1991) Possible involvement of nitric oxide in long-term potentiation. Eur J Pharmacol 199:379–381.

Bredt DS, Snyder SH (1989) Nitric oxide mediates glutamate-linked enhancement of cGMP levels in the cerebellum. Proc Natl Acad Sci USA 86:9030–9033.

Bredt DS, Snyder SH (1990) Isolation of nitric oxide synthase, a calmodulin-requiring enzyme. Proc Natl Acad Sci USA 87:682–685.

Brenman JE, Chao DS, Gee SH, McGee AW, Craven SE, Santillano DR, Wu A, Huang F, Xia H, Peters MF, Froehner SC, Bredt DS (1996) Interaction of nitric oxide synthase with the postsynaptic density protein PSD-95 and α1-syntrophin mediated by PDZ domains. Cell 84:757–767.

Broillet M-C, Randin O, Chatton J-Y (2001) Photoactivation and calcium sensitivity of the fluorescent NO indicator 4,5-diaminofluorescein (DAF-2): implications for cellular NO imaging. FEBS Lett 491:227–232.

Bronner C, Landry Y, Fonteneau PA, Kuhry JG (1986) Fluorescent hydrophobic probe used for monitoring the kinetics of exocytosis phenomena. Biochemistry 25:2149–2154.

Calabresi P, Gubellini P, Centonze D, Sancesario G, Morello M, Giorgi M, Pisani A, Bernardi G (1999) A critical role of the nitric oxide/cGMP pathway in corticostriatal long-term depression. J Neurosci 19:2489–2499.

Casado M, Dieudonne S, Ascher P (2000) Presynaptic *N*-methyl-D-aspartate receptors at the parallel fiber-Purkinje cell synapse. Proc Natl Acad Sci USA 97:11593–11597.

Christopherson KS, Hillier BJ, Lim WA, Bredt DS (1999) PSD-95 assembles a ternary complex with the *N*-methyl-D-aspartic acid receptor and a bivalent neuronal NO synthase PSD domain. J Biol Chem 274:27467–27473.

Crepel F, Audinat E, Daniel H, Hemart N, Jaillard D, Rossier J, Lambolez B (1994) Cellular locus of the nitric oxide-synthase involved in cerebellar long-term depression induced by high external potassium concentration. Neuropharmacology 33:1399–1405.

DeVente J, Bol JGJM, Berkelmans HS, Schipper J, Steinbusch HMW (1990) Immunocytochemistry of cGMP in the cerebellum of the immature, adult, and aged rat: the involvement of nitric oxide: a micropharmacological study. Eur J Neurosci 2:845–862.

Förstermann U, Gath I (1996) Purification of isoforms of nitric oxide synthase. Methods Enzymol 268:334–349.

Fujii S, Suzuki Y, Yoshimura T, Kamada H (1998) In vivo three-dimensional EPR imaging of nitric oxide production from isosorbide dinitrate in mice. Am J Physiol 274:G857–862.

Furuya S, Makino A, Hirabayashi Y (1998) An improved method for culturing cerebellar Purkinje cells with differentiated dendrites under a mixed monolayer setting. Brain Res Protocols 3:192–198.

Gally JA, Montague PR, Reeke GN, Edelman GM (1990) The NO hypothesis: possible effects of a short-lived, rapidly diffusible signal in the development and function of the nervous system. Proc Natl Acad Sci USA 87:3547–3551.

Garthwaite J, Charles SL, Chess-Williams C (1988) Endothelium-derived relaxing factor release on activation of NMDA receptors suggests role as intercellular messenger in the brain. Nature 336:385–388.

Garthwaite J (1991) Glutamate, nitric oxide and cell-cell signalling in the nervous system. Trends Neurosci 14:60–67.

Gudi T, Casteel DE, Vinson C, Ross GR, Pilz RB (2000) NO activation of *fos* promoter elements requires nuclear translocation of G-kinase and CREB phosphorylation but is independent of MAP kinase activation. Oncogene 19:6324–6333.

Hartell NA (1996) Strong activation of parallel fibers produces localized calcium transients and a form of LTD that spreads to distant synapses. Neuron 16:801–810.

Hartell NA, Furuya S, Jacoby S, Okada D (2001) Intercellular action of nitric oxide increases cGMP in cerebellar Purkinje cells. Neuroreport 12:25–28.

Hawkes H, Turner RW (1994) Compartmentation of NADPH-diaphorase activity in the mouse cerebellar cortex. J Comp Neurol 346:499–516.

Hunt CA, Schenker LJ, Kennedy MB (1996) PSD-95 is associated with the postsynaptic density and not with the presynaptic membrane at forebrain synapses. J Neurosci 16:1380–1388.

Ito M (1984) The cerebellum and neural control. New York: Raven Press.

Jourd'heuil D (2002) Increased nitric oxide-dependent nitrosylation of 4,5-diaminofluorescein by oxidants: implications for the measurement of intracellular nitric oxide. Free Radic Biol Med 33:676–684.

Kimura S, Uchiyama S, Takahashi HE, Shibuki K (1998) cAMP-dependent long-term potentiation of nitric oxide release from cerebellar parallel fibers in rats. J Neurosci 18:8551–8558.

Kojima H, Nakatsubo N, Kikuchi K, Kawahara S, Kirino Y, Nagoshi H, Hirata Y, Nagano T (1998) Detection and imaging of nitric oxide with novel fluorescent indicators: diaminofluoresceins. Anal Chem 70:2446–2453.

Kojima H, Hirotani M, Nakatsubo N, Kikuchi K, Urano Y, Higuchi T, Hirata Y, Nagano T (2001) Bioimaging of nitric oxide with fluorescent indicators based on rhodamine chromophore. Anal Chem 73:1967–1973.

Krekelberg B, Taylor JG (1996) Nitric oxide in cortical map formation. J Chem Neuroanat 10:191–196.

Lancaster JR (1994) Simulation of the diffusion and reaction of endogenously produced nitric oxide. Proc Natl Acad Sci USA 91:8137–8141.

Lev-Ram V, Makings LR, Keitz PF, Kao JP, Tsien RY (1995) Long-term depression in cerebellar Purkinje neurons results from coincidence of nitric oxide and depolarization-induced Ca^{2+} transients. Neuron 15:407–415.

Malinski T, Taha Z (1992) Nitric oxide release from a single cell measured in situ by a porphyrinic-based microsensor. Nature 358:676–678.

Miyata M, Okada D, Hashiimoto K, Kano M, Ito M (1999) Corticotropin-releasing factor plays a permissive role in cerebellar long-term depression. Neuron 22:763–775.

Oberdick J, Baader SL, Schilling K (1998) From zebra stripes to postal zones: deciphering patterns of gene expression in the cerebellum. Trends Neurosci 21:383–390.

Okada D (1992) Two pathways of cyclic GMP production through glutamate receptor mediated nitric oxide synthesis. J Neurochem 59:1203–1210.

Okada D (2000) Neutral red as a hydrophobic probe for neuronal activity monitoring. J Neurosci Methods 101:85–92.

Petralia RS, Yokotani N, Wenthold RJ (1994a) The NMDA receptor subunits NR2A and NR2B show histological and ultrastructural

localization patterns similar to those of NR1. J Neurosci 14:6102–6120.

Petralia RS, Yokotani N, Wenthold RJ (1994b) Light and electron microscope distribution of the NMDA receptor subunit NMDAR1 in rat nervous system using a selective anti-peptide antibody. J Neurosci 14:667–696.

Peunova N, Enikolopov G (1993) Amplification of calcium-induced gene transcription by nitric oxide in neuronal cells. Nature 364:450–453.

Räthel TR, Leikert JF, Vollmar AM, Dirsch VM (2003) Application of 4,5-diaminofluorescein to reliably measure nitric oxide released from endothelial cells in vitro. Biol Proc Online 5:136–142.

Robello M, Amico C, Bucossi G, Cupello A, Rapalino MV, Thellung S (1996) Nitric oxide and GABAA receptor function in the rat cerebral cortex and cerebellar granule cells. Neuroscience 74:99–105.

Rodrigo J, Springall DR, Uttenthal O, Bentura ML, Abadia-Molina F, Riveros-Moreno V, Martinez-Murillo R, Polak JM, Moncada S (1994) Localization of nitric oxide synthase in the adult rat brain. Phil Trans R Soc Lond B 345:175–221.

Sattler R, Xiong Z, Lu W-Y, Hafner M, MacDonald JF, Tymianski M (1999) Specific coupling of NMDA receptor activation to nitric oxide neurotoxicity by PSD-95 protein. Science 284:1845–1848.

Schuman EM, Madison DV (1994) Nitric oxide and synaptic function. Annu Rev Neurosci 17:153–183.

Shen KZ, Cox BA, Johnson SW (1997) L-Arginine potentiates GABA-mediated synaptic transmission by a nitric oxide-dependent mechanism in rat dopamine neurons. Neuroscience 79:649–658.

Shibuki K, Kimura S (1997) Dynamic properties of nitric oxide release from parallel fibres in rat cerebellar slices. J Physiol (Lond) 498: 443–452.

Shibuki K, Okada D (1991) Endogenous nitric oxide release required for long-term synaptic depression in the cerebellum. Nature 349: 326–328.

Skeberdis VA, Lan J, Opitz T, Zheng X, Bennett MV, Zukin RS (2001) mGluR1-mediated potentiation of NMDA receptors involves a rise in intracellular calcium and activation of protein kinase C. Neuropharmacology 40:856–865.

Southam E, East SJ, Garthwaite J (1991) Excitatory amino acid receptors coupled to the nitric oxide/cyclic GMP pathway in rat cerebellum during development. J Neurochem 56:2072–2081.

Suzuki N, Kojima H, Urano Y, Kikuchi K, Hirata Y, Nagano T (2002) Orthogonality of calcium concentration and ability of 4,5-diaminofluorescein to detect NO. J Biol Chem 277:47–49.

Tanaka M, Yoshida S, Yano M, Hanaoka F (1994) Roles of endogenous nitric oxide in cerebellar cortical development in slice cultures. Neuroreport 5:2049–2052.

Watanabe M, Mishina M, Inoue Y (1994) Distinct spatiotemporal expressions of five NMDA receptor channel subunit mRNAs in the cerebellum. J Comp Neurol 343:513–519.

Wood J, Garthwaite J (1994) Models of the diffusional spread of nitric oxide: implications for neural nitric oxide signalling and its pharmacological properties. Neuropharmacology 33:1235–1244.

Wu HH, Williams CV, McLoon SC (1994) Involvement of nitric oxide in the elimination of a transient retinotectal projection in development. Science 265:1593–1596.

Yan XX, Jen LS, Garey LJ (1993) Parasagittal patches in the granular layer of the developing and adult rat cerebellum as demonstrated by NADPH-diaphorase histochemistry. Neuroreport 4:1227–1230.

Zhang X, Kim WS, Hatcher N, Potgieter K, Moroz LL, Gillette R, Sweedler JV (2002) Interfering with nitric oxide measurements: 4,5-diaminofulorescein reacts with dehydroascorbic acid and ascorbic acid. J Biol Chem 277:48472–48478.

(Accepted 23 January 2004)

J|A|C|S
ARTICLES
Published on Web 09/10/2004

Development of a Zinc Ion-Selective Luminescent Lanthanide Chemosensor for Biological Applications

Kenjiro Hanaoka,† Kazuya Kikuchi,*,†,‡ Hirotatsu Kojima,† Yasuteru Urano,† and Tetsuo Nagano*,†

Contribution from the Graduate School of Pharmaceutical Sciences, The University of Tokyo, 7-3-1 Hongo, Bunkyo-ku, Tokyo 113-0033, Japan, and Presto, JST Corporation, Kawaguchi, Saitama 332-0012, Japan

Received May 25, 2004; E-mail: tlong@mol.f.u-tokyo.ac.jp (T.N.); kkikuchi@mol.f.u-tokyo.ac.jp (K.K.)

Abstract: Detection of chelatable zinc (Zn^{2+}) in biological studies has attracted much attention recently, because chelatable Zn^{2+} plays important roles in many biological systems. Lanthanide complexes (Eu^{3+}, Tb^{3+}, etc.) have excellent spectroscopic properties for biological applications, such as long luminescence lifetimes of the order of milliseconds, a large Stoke's shift of >200 nm, and high water solubility. Herein, we present the design and synthesis of a novel lanthanide sensor molecule, **[Eu-7]**, for detecting Zn^{2+}. This europium (Eu^{3+}) complex employs a quinolyl ligand as both a chromophore and an acceptor for Zn^{2+}. Upon addition of Zn^{2+} to a solution of **[Eu-7]**, the luminescence of Eu^{3+} is strongly enhanced, with high selectivity for Zn^{2+} over other biologically relevant metal cations. One of the important advantages of **[Eu-7]** is that this complex can be excited with longer excitation wavelengths (around 340 nm) as compared with previously reported Zn^{2+}-sensitive luminescent lamthanide sensors, whose excitation wavelength is at too high an energy level for biological applications. The usefulness of **[Eu-7]** for monitoring Zn^{2+} changes in living HeLa cells was confirmed. This novel Zn^{2+}-selective luminescent lanthanide chemosensor **[Eu-7]** should be an excellent lead compound for the development of a range of novel luminescent lanthanide chemosensors for biological applications.

Introduction

Zinc (Zn^{2+}) is the second most abundant heavy metal ion after iron in the human body, and the total zinc ion concentration in serum is of the order of 10 μM.[1] Zn^{2+} is an essential component of many enzymes (e.g., carbonic anhydrase), and also plays critical roles in maintaining key structural features of gene transcription proteins (e.g., zinc finger proteins).[2] Moreover, chelatable Zn^{2+} is present at especially high concentrations in brain,[3] pancreas,[4] and spermatozoa.[5] Chelatable Zn^{2+} regulates neuronal transmission in excitatory nerve terminals,[3] suppresses apoptosis,[6] contributes to neuronal injury in certain acute conditions,[7] epilepsy,[8] and transient global ischemia,[9] and induces the formation of β-amyloid,[10] which is reported to be related to the etiology of Alzheimer's disease. Although many reports describe the significance of chelatable Zn^{2+} in biological systems, its mechanisms of action are less well understood than those of other cations, such as Ca^{2+}, Na^{+}, and K^{+}. Therefore, there is considerable interest in detecting chelatable Zn^{2+} in biological systems.[11]

So far, several Zn^{2+}-selective fluorescent sensor molecules have been reported.[12] However, novel types of Zn^{2+}-sensitive fluorescent sensor molecules are needed for studies on biological phenomena, and several new types of sensors that are designed for ratiometric measurement,[13] or that are peptide- or protein-based,[14] have recently been introduced. Ratiometric measure-

† The University of Tokyo.
‡ Presto, JST Corporation.

(1) Paker, M. M.; Humaller, F. L.; Mahler, D. J. *Clin. Chem.* **1967**, *13*, 40–48.
(2) (a) Vallee, B. L.; Falchuk, K. H. *Physiol. Rev.* **1993**, *73*, 79–118. (b) Berg, J. M.; Shi, Y. *Science* **1996**, *271*, 1081–1085.
(3) Frederickson, C. J. *Int. Rev. Neurobiol.* **1989**, *31*, 145–238.
(4) Zalewski, P. D.; Millard, S. H.; Forbes, I. J.; Kapaniris, O.; Slavotinek, A.; Betts, W. H.; Ward, A. D.; Lincoln, S. F.; Mahadevan, I. *J. Histochem. Cytochem.* **1994**, *42*, 877–884.
(5) Zalewski, P. D.; Jian, X.; Soon, L. L. L.; Breed, W. G.; Seamark, R. F.; Lincoln, S. F.; Ward, A. D.; Sun, F. Z. *Reprod. Fertil. Dev.* **1996**, *8*, 1097–1105.
(6) Truong-Tran, A. Q.; Ho, L. H.; Chai, F.; Zalewski, P. D. *J. Nutr.* **2000**, *130*, 1459S-1466S.
(7) Choi, D. W.; Koh, J. Y. *Annu. Rev. Neurosci.* **1998**, *21*, 347–375.
(8) Frederickson, C. J.; Hernandez, M. D.; McGinty, J. F. *Brain Res.* **1989**, *480*, 317–321.
(9) Koh, J. Y.; Suh, S. W.; Gwag, B. J.; He, Y. Y.; Hsu, C. Y.; Choi, D. W. *Science* **1996**, *272*, 1013–1016.
(10) Bush, A. I.; Pettingell, W. H.; Multhaup, G.; Paradis, M. D.; Vonsattel, J. P.; Gusella, J. F.; Beyreuther, K.; Masters, C. L.; Tanzi, R. E. *Science* **1994**, *265*, 1464–1467.
(11) (a) Kikuchi, K.; Komatsu K.; Nagano T. *Curr. Opin. Chem. Biol.* **2004**, *8*, 182–191. (b) Jiang, P.; Guo, Z. *Coord. Chem. Rev.* **2004**, *248*, 205–229.
(12) (a) Frederickson, C. J.; Kasarskis, E. J.; Ringo, D.; Frederickson, R. E. *J. Neurosci. Methods* **1987**, *20*, 91–103. (b) Zalewski, P. D.; Forbes, I. J.; Betts, W. H. *Biochem. J.* **1993**, *296*, 403–408. (c) Hirano, T.; Kikuchi, K.; Urano, Y.; Nagano, T. *J. Am. Chem. Soc.* **2002**, *124*, 6555–6562. (d) Walkup, G. K.; Burdette, S. C.; Lippard, S. J.; Tsien, R. Y. *J. Am. Chem. Soc.* **2000**, *122*, 5644–5645. (e) Haugland, R. P. *Handbook of Fluorescent Probes and Research Chemicals*, 6th ed.; Molecular Probes, Inc.; Eugene, OR, 1996; pp 531–540. (f) Hendrickson K. M.; Geue, J. P.; Wyness, O.; Lincoln, S. F.; Ward, A. D. *J. Am. Chem. Soc.* **2003**, *125*, 3889–3895. (g) Gee, K. R.; Zhou, Z. L.; Qian, W. J.; Kennedy, R. *J. Am. Chem. Soc.* **2002**, *124*, 776–778. (h) Burdette, S. C.; Frederickson, C. J.; Bu, W.; Lippard, S. J. *J. Am. Chem. Soc.* **2003**, *125*, 1778–1787.
(13) (a) Henary, M. M.; Wu, Y.; Fahrni, C. J. *Chem. Eur. J.* **2004**, *10*, 3015–3025. (b) Taki, M.; Wolford, J. L.; O'Halloran, T. V. *J. Am. Chem. Soc.* **2004**, *126*, 712–713. (c) Woodroofe, C. C.; Lippard, S. J. *J. Am. Chem. Soc.* **2003**, *125*, 11458–11459. (d) Maruyama, S.; Kikuchi, K.; Hirano, T.; Urano, Y.; Nagano, T. *J. Am. Chem. Soc.* **2002**, *124*, 10650–10651.

10.1021/ja0469333 CCC: $27.50

ment in particular enables more precise analysis of Zn^{2+} concentrations. The other approach for precise analyses is time-resolved fluorescence (TRF) measurement, which offers a better signal-to-noise ratio. Luminescent lanthanide complexes are suitable for TRF measurement. So, our interest in Zn^{2+}-selective fluorescent sensor molecules was directed toward luminescent lanthanide complexes, in particular complexes of the europium and terbium trivalent ions (Eu^{3+} and Tb^{3+}). These complexes have large Stoke's shifts (>200 nm), long luminescence lifetimes of the order of milliseconds, and high water solubility,[15] whereas the typical organic fluorescent compounds possess small Stoke's shifts (Stoke's shifts of fluorescein and rhodamine are ~25 and ~20 nm, respectively)[12c-e,16] and short fluorescence lifetimes in the nanosecond region. The long-lived luminescence of the lanthanides has the advantage that short-lived background fluorescence and scattered light decay to negligible levels when a pulse of excitation light is applied and the emitted light is collected after an appropriate delay time. For these reasons, sensitization of lanthanide luminescence has been exploited for a number of useful signaling systems for time-resolved assays in the fields of medicine, biotechnology, and biological science.[17] The lanthanide f−f transitions have low absorbance, so the ligand structure requires a sensitizing chromophore for high luminescence.[18] Absorption by the chromophore results in effective population of its triplet level, and efficient intramolecular energy transfer occurs from the excited chromophore to the lanthanide metal, whereby the metal becomes excited to the emission state (Scheme 1).[15a,17g,18b] By means of appropriate chromophore design, it is possible to develop luminescent lanthanide complexes which can be used to sense various biological molecules.

There are only a few reports about lanthanide-based luminescent chemosensors for the detection of Zn^{2+}.[19] Parker and co-workers have developed a luminescent lanthanide agent which binds Zn^{2+} with an apparent dissociation constant K_d of 0.6 μM (295 K, pH 7.3).[19a,c] We employed a different design approach for a ligand and an antenna in a previous report, and

Scheme 1. (a) Schematic View of a Chromophore Incorporated into a Europium Emitter[a] and (b) the General Chromophore-to-Europium Ion Sensitization Process[b]

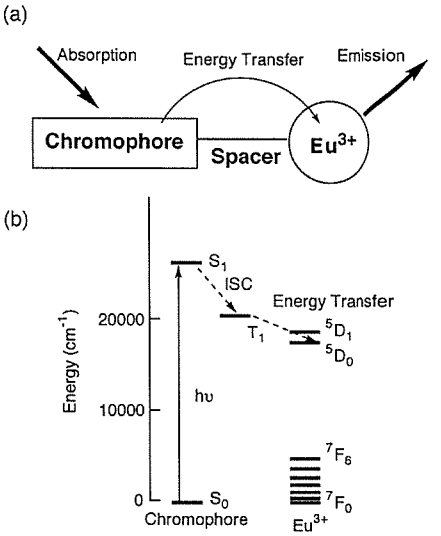

[a] The emission from Eu^{3+} after excitation of the chromophore is shown. [b] Light absorption and lowest-lying singlet excited state (S_1) formation at the sensitizing chromophore are followed by intersystem crossing (ISC), resulting in population of the lowest-lying triplet excited state (T_1). Subsequent chromophore-to-Eu^{3+} energy transfer leads to population of a metal-centered level, which deactivates from Eu^{3+}-emitting states to the relevant ground states.

the novel lanthanide complexes obtained showed a large enhancement of luminescence upon Zn^{2+} addition with an apparent dissociation constant K_d of 2.6 nM (295 K, pH 7.4).[19b] However, these compounds are unsuitable for biological applications, because of their short excitation wavelength, small emission enhancement, inconvenient pH sensitivity, insufficient selectivity for Zn^{2+}, etc. So, it is necessary to develop sensors with a longer excitation wavelength for biological applications without losing the high selectivity and high affinity for Zn^{2+}. Moreover, development of a simple sensor switch for Zn^{2+}, which would serve as both chromophore and Zn^{2+} receptor, would be useful. From this background, we set out to develop a novel lanthanide complex which can detect Zn^{2+} in biological systems, in the relevant concentration range.

Here we report the design and synthesis of the novel Zn^{2+}-sensitive luminescent lanthanide chemosensor **[Eu-7]**; upon complexation with Zn^{2+}, it exhibits strong, long-lived luminescence (of the order of milliseconds), and it also offers a large Stoke's shift (>250 nm), high water-solubility, and high selectivity for Zn^{2+} (Figure 1).

Results and Discussion

Design and Synthesis of [Eu-7] and [Gd-7]. *N,N,N′,N′*-Tetrakis(2-pyridylmethyl)ethylenediamine[20] (TPEN) shows high selectivity for Zn^{2+} over other metal ions found under physiological conditions, such as Ca^{2+} and Mg^{2+}. Accordingly, we

(14) (a) Thompson, R. B.; Cramer, M. L.; Bozym, R.; Fierke, C. A. *J. Biomed. Opt.* **2002**, *7*, 555−560. (b) Shults, M. D.; Pearce, D. A.; Imperiali, B. *J. Am. Chem. Soc.* **2003**, *125*, 10591−10597. (c) Barondeau, D. P.; Kassmann, C. J.; Tainer, J. A.; Getzoff, E. D. *J. Am. Chem. Soc.* **2002**, *124*, 3522−3524.

(15) (a) Parker, D.; Williams, J. A. G. *J. Chem. Soc., Dalton Trans.* **1996**, 3613−3628. (b) Li, M.; Selvin, P. R. *J. Am. Chem. Soc.* **1995**, *117*, 8132−8138. (c) Beck, J. B.; Rowan, S. J. *J. Am. Chem. Soc.* **2003**, *125*, 13922−13923. (d) Franz, K. J.; Nitz, M.; Imperiali, B. *ChemBioChem* **2003**, *4*, 265−271. (e) Liu, W.; Jiao, T.; Li, Y.; Liu, Q.; Tan, M.; Wang, H.; Wang, L. *J. Am. Chem. Soc.* **2004**, *126*, 2280−2281. (f) Weibel, N.; Charbonnière, L. J.; Guardigli, M.; Roda, A.; Ziessel, R. *J. Am. Chem. Soc.* **2004**, *126*, 4888−4896. (g) Alpha, B.; Lehn, J. M.; Mathis, G. *Angew. Chem., Int. Ed. Engl.* **1987**, *26*, 266−267. (h) Petoud, S.; Cohen, S. M.; Bünzli, J. C. G.; Raymond, K. N. *J. Am. Chem. Soc.* **2003**, *125*, 13324−13325. (i) Maffeo, D.; Williams, J. A. G. *Inorg. Chim. Acta* **2003**, *355*, 127−136.

(16) Mizukami, S.; Kikuchi, K.; Higuchi, T.; Urano, Y.; Mashima, T.; Tsuruo, T.; Nagano, T. *FEBS Lett.* **1999**, *453*, 356−360.

(17) (a) Kolb, A. J.; Kaplita, P. V.; Hayes, D. J.; Park, Y. W.; Pernell, C.; Major, J. S.; Mathis, G *Drug Discovery Today* **1998**, *3*, 333−342. (b) Enomoto, K.; Araki, A.; Nakajima, T.; Ohta, H.; Dohi, K.; Préaudat, M.; Seguin, P.; Mathis, G.; Suzuki, R.; Kominami, G.; Takemoto, H. *J. Pharm. Biomed. Anal.* **2002**, *28*, 73−79. (c) Beeby, A.; Botchway, S. W.; Clarkson, I. M.; Faulkner, S.; Parker, A. W.; Parker, D.; Williams, J. A. G. *J. Photochem. Photobiol. B: Biology* **2000**, *57*, 83−89. (d) Frias, J. C.; Bobba, G.; Cann, M. J.; Hutchison, C. J.; Parker, D. *Org. Biomol. Chem.* **2003**, *1*, 905−907. (e) Barrios, A. M.; Craik, C. S. *Bioorg. Med. Chem. Lett.* **2002**, *12*, 3619−3623. (f) Vereb, G.; Jares-Erijman, E.; Selvin, P. R.; Jovin, T. M. *Biophys. J.* **1998**, *74*, 2210−2222. (g) Matsumoto, K.; Nojima, T.; Sano, H.; Majima, K. *Macromol. Symp.* **2002**, *186*, 117−121. (h) Karvinen, J.; Hurskainen, P.; Gopalakrishnan, S.; Burns, D.; Warrior, U.; Hemmilä, I. *J. Biomol. Screen.* **2002**, *7*, 223−231. (i) Préaudat, M.; Ouled-Diaf, J.; Alpha-Bazin, B.; Mathis, G.; Mitsugi, T.; Aono, Y.; Takahashi, K.; Takemoto, H. *J. Biomol. Screen.* **2002**, *7*, 267−274. (j) Lin, Z.; Wu, M.; Schäferling, M.; Wolfbeis, O. S. *Angew. Chem., Int. Ed.* **2004**, *43*, 1735−1738.

(18) (a) Parker, D.; Dickins, R. S.; Puschmann, H.; Crossland, C.; Howard, J. A. K. *Chem. Rev.* **2002**, *102*, 1977−2010. (b) Quici, S.; Marzanni, G.; Carazzini, M.; Anelli, P. L.; Botta, M.; Gianolio, E.; Accorsi, G.; Armaroli, N.; Barigelletti, F. *Inorg. Chem.* **2002**, *41*, 2777−2784. (c) Latva, M.; Takalo, H.; Mukkala, V. M.; Matachescu, C.; Rodríguez-Ubis, J. C.; Kankare, J. *J. Lumin.* **1997**, *75*, 149−169. (d) Dadabhoy, A.; Faulkner, S.; Sammes, P. G. *J. Chem. Soc., Perkin Trans. 2* **2002**, 348−357.

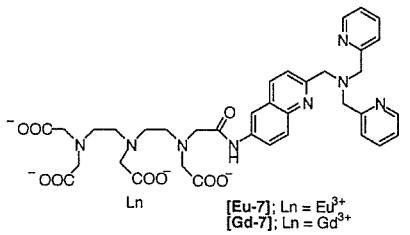

Figure 1. Structures of Eu^{3+} and Gd^{3+} *N*-{*N*-[2-*N*,*N*-bis(2-pyridylmethyl)-aminomethylquinolin-6-yl]carbamoylmethyl}-*N*,*N*′,*N*″,*N*‴-diethylenetriaminetetraacetic acid complexes: **[Eu-7]** and **[Gd-7]**.

designed a novel sensitive luminescent sensor for Zn^{2+} **[Eu-7]** by the combination of Eu^{3+}–diethylenetriaminepentaacetic acid (DTPA) complex and a quinoline-containing TPEN-based ligand for Zn^{2+}. The quinoline chromophore was selected as an antenna and a ligand, because quinoline has a longer excitation wavelength (>300 nm)[21] than pyridine and can coordinate to metal ions.

In the structure of **[Eu-7]**, the quinolyl chromophore is fixed close to the Eu^{3+} ion, allowing it to function as an antenna. The synthetic schemes for the lanthanide complexes, **[Eu-7]** and **[Gd-7]**, and details of the chemical characterization of compounds are provided in the Supporting Information.

Spectroscopic Characteristics of a Solution of [Eu-7] upon Addition of Zn^{2+}. The complex **[Eu-7]** in aqueous solution was characterized by a time-delayed luminescence spectrum with a delay time of 0.05 ms. The time-resolved luminescence emission intensity of **[Eu-7]** (50 μM) increased significantly (8.5-fold) upon addition of 1.0 equiv of Zn^{2+}, with a large Stoke's shift of >250 nm. The emission intensity remained at a plateau in the presence of an excess of Zn^{2+} (Figure 2). The luminescence emission displayed three bands at 579, 593, and 614 nm, corresponding to the deactivation from the $^5D_0$ excited state to $^7F_0$, $^7F_1$, and $^7F_2$ ground state, respectively.[18b,21b] The UV–vis absorption spectral change was monitored during Zn^{2+} addition. The absorption spectrum of **[Eu-7]** without Zn^{2+} had λ_{max} = 249 nm and broad bands at 330 and 318 nm, tailing out to 350 nm (Figure 3). The absorption spectrum of **[Eu-7]** changed upon addition of Zn^{2+} (0–1.0 equiv), with three isosbestic points at 334, 268, and 248 nm, and then remained at a plateau upon further addition of Zn^{2+} (Figure 3 and Figure S4), in accordance with the time-resolved luminescence spectra (Figure 2). The three peaks (330, 318, and 249 nm) of absorption changed to two peaks (320 and 253 nm) upon Zn^{2+} addition. The absorption wavelength changes between 300 and 350 nm were supposed to be due to the photophysical property change of the quinolyl moiety with Zn^{2+} chelation, whereas pyridine–Zn^{2+} coordination resulted in changes below 300 nm.[19b] Thus, 1:1 complex stoichiometry was observed in both the absorption and the luminescence emission spectra of **[Eu-7]**. The Job's plot using the luminescence emission intensity of Eu^{3+} at 614 nm for the complex of **[Eu-7]** and Zn^{2+} also indicated the presence of the 1:1 complex (see Supporting Information).[22] For **[Eu-7]** (20 μM), the fluorescence emission spectra were measured without a delay time, with excitation at 320 nm (Figure 4). In the fluorescence emission of **[Eu-7]**, one band with a short lifetime appeared at 397 nm with a concomitant linear fluorescence increase following addition of Zn^{2+} at between 0 and 1.0 equiv to **[Eu-7]**, and it remained at a plateau with further Zn^{2+} addition (Figure S6). The short-lived fluorescence at 397 nm can be ascribed to direct emission from the quinolyl moiety of **[Eu-7]**.[21a,b] All these results can be rationalized in terms of 1:1 complex formation of **[Eu-7]** with Zn^{2+}, via the quinolyl ligand.

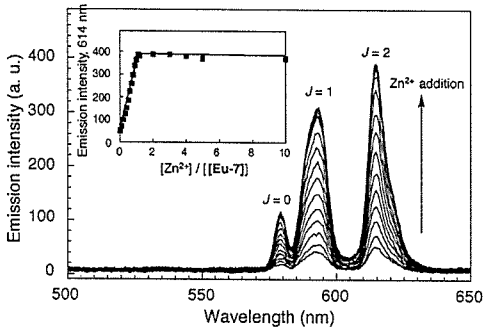

Figure 2. Time-delayed emission spectra (excitation at 320 nm) of **[Eu-7]** (50 μM) in the presence of various concentrations of Zn^{2+}: 0, 0.1, 0.2, 0.3, 0.4, 0.5, 0.6, 0.7, 0.8, 0.9, 1.0, 1.1, 1.2, 2.0, 3.0, 4.0, 5.0, and 10.0 equiv of Zn^{2+} with respect to **[Eu-7]**. These spectra were measured at pH 7.4 (100 mM HEPES buffer) and 22 °C using a delay time of 0.05 ms and a gate time of 1.00 ms. The inset shows the changes of the luminescence intensity at λ = 614 nm. The bands arise from $^5D_0 \rightarrow {}^7F_J$ transitions; the J values of the bands are labeled.

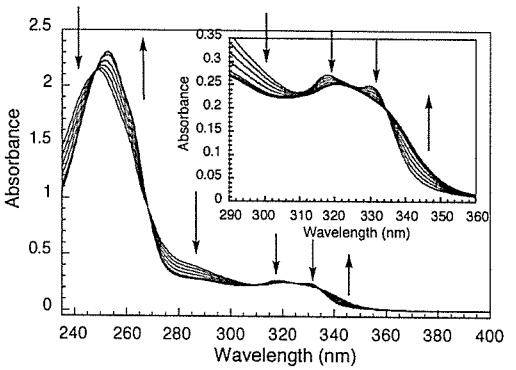

Figure 3. Absorbance spectra of 50 μM aqueous solution (100 mM HEPES buffer; pH 7.4) of **[Eu-7]** at 22 °C upon addition of aliquots of Zn^{2+}, which was added as $ZnSO_4$: 0, 0.2, 0.4, 0.6, 0.8, 1.0, 2.0, 3.0, 4.0, 5.0, and 10.0 equiv of Zn^{2+} with respect to **[Eu-7]**. The inset shows the spectra magnified between 290 and 360 nm.

Luminescence and Chemical Properties of [Eu-7] and [Gd-7]. The luminescence and chemical properties of **[Eu-7]** and **[Gd-7]** are listed in Table 1. **[Eu-7]** and **[Gd-7]**, even at 10 mM, were highly water-soluble. The phosphorescence spectra of **[Gd-7]** were measured in MeOH:EtOH = 1:1 at 77 K in the absence and in the presence of Zn^{2+}. The triplet energy levels for free and Zn^{2+}-bound **[Gd-7]** were around 20 790 and 20 576

(19) (a) Reany, O.; Gunnlaugsson, T.; Parker, D. *J. Chem. Soc., Perkin Trans. 2* **2000**, 1819–1831. (b) Hanaoka, K.; Kikuchi, K.; Kojima, H.; Urano, Y.; Nagano, T. *Angew. Chem., Int. Ed.* **2003**, *42*, 2996–2999. (c) Reany, O.; Gunnlaugsson, T.; Parker, D. *Chem. Commun.* **2000**, 473–474.

(20) Sillén, L. G.; Martell, A. E. *Stability Constants of Metal-Ion Complexes*; Special Publication No. 17; The Chemical Society: Burlington House, London, 1964.

(21) (a) Gunnlaugsson, T. *Tetrahedron Lett.* **2001**, *42*, 8901–8905. (b) Gunnlaugsson, T.; MacDónaill, D. A.; Parker, D. *J. Am. Chem. Soc.* **2001**, *123*, 12866–12876. (c) Manning, H. C.; Goebel, T.; Marx, J. N.; Bornhop, D. J. *Org. Lett.* **2002**, *4*, 1075–1078. (d) Jotterand, N.; Pearce, D. A.; Imperiali, B. *J. Org. Chem.* **2001**, *66*, 3224–3228.

(22) Nabeshima, T.; Tsukada, N.; Nishijima, K.; Ohshiro, H.; Yano, Y. *J. Org. Chem.* **1996**, *61*, 4342–4350.

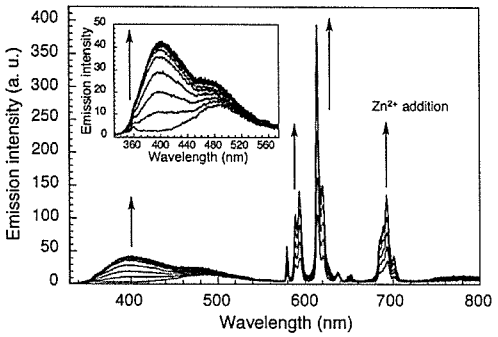

Figure 4. Fluorescence spectra of **[Eu-7]** (20 μM) in 100 mM HEPES buffer at pH 7.4 without a delay time upon the addition of increasing amounts of Zn^{2+}: 0, 0.2, 0.4, 0.6, 0.8, 1.0, 2.0, 3.0, 4.0, 5.0, and 10.0 equiv of Zn^{2+} with respect to **[Eu-7]**. Excitation at 320 nm, 22 °C. The inset shows the spectra magnified between 330 and 575 nm.

Table 1. Luminescence and Chemical Properties

		ϕ (%)[b]		τ_{H_2O} (ms)[c]		τ_{D_2O} (ms)[d]		q[e]	
	apparent K_d for Zn^{2+} (nM)[a]	free	Zn^{2+} complex	free	Zn^{2+} complex	free	Zn^{2+} compex	free	Zn^{2+} complex
[Eu-7]	59	0.9	7.4	0.52	0.58	2.03	2.23	1.42	1.22

	triplet state energy (cm^{-1})[f]		r_1 (mM^{-1} s^{-1})[g]	
	free	Zn^{2+} complex	free	Zn^{2+} complex
[Gd-7]	20790	20576	6.05	5.81

[a] $[Zn^{2+}]$ was controlled by using Zn^{2+}/NTA systems below 398 nM free Zn^{2+} and unbuffered Zn^{2+} above 200 μM free Zn^{2+}. The buffer contained 100 mM HEPES, pH 7.4, I = 0.1 ($NaNO_3$). [b] Quantum yields were calculated using $[Ru(bipy)_3]Cl_2$ (bipy = 2,2′-bipyridine; ϕ = 0.028 in water) as a standard, and measured in 100 mM HEPES buffer at pH 7.4, 25 °C. [c] In H_2O-based buffer (100 mM HEPES buffer; pH 7.4). [d] In D_2O-based buffer (100 mM HEPES buffer; pD 7.4). [e] q values were estimated using the equation $q^{Eu} = 1.2(\tau_{H_2O}{}^{-1} - \tau_{D_2O}{}^{-1} - 0.25)$, which allows for the contribution of unbound water molecules.[23] [f] In MeOH:EtOH = 1:1 at 77 K. [g] The R_1 relaxivity as measured at 20 MHz and 25 °C in 100 mM HEPES buffer (pH 7.4).

cm^{-1}, respectively, and both were sufficiently close to the $^5D_0$ level, the excited state, of Eu^{3+} (E = 17 250 cm^{-1}).[23] The luminescence quantum yield (ϕ) was 0.9% before addition of Zn^{2+} and was increased 8.2-fold to 7.4% by Zn^{2+} addition, under air-equilibrated conditions. This luminescence quantum yield is sufficiently large for luminescence detection. Further, the binding affinity for Zn^{2+} was assessed by using the luminescence intensity. The affinity of **[Eu-7]** for Zn^{2+} ions was measured at pH 7.4, 22 °C, in a high salt background (100 mM HEPES buffer, I = 0.1 ($NaNO_3$)). The apparent dissociation constant K_d for Zn^{2+} was calculated to be 59 nM. This K_d value for Zn^{2+} was larger than that reported for tris(2-pyridylmethyl)-amine (TPA) (K_d = 0.014 nM; pH = 7.4, 298 K, I = 0.1),[24] probably due to a larger steric repulsion in the case of the quinolyl substituent than the pyridyl substituent, but the value is still sufficiently small for biological applications.[25] Measurements of the decay rate constants of the Eu^{3+} excited state were carried out in both H_2O and D_2O, in the absence and in the presence of Zn^{2+} (see Supporting Information). The luminescence lifetimes of **[Eu-7]** were found to be 0.52 (without Zn^{2+}) and 0.58 (with Zn^{2+}) ms in H_2O (τ_{H_2O}), and 2.03 (without Zn^{2+}) and 2.23 (with Zn^{2+}) ms in D_2O (τ_{D_2O}). These values indicated that the numbers of coordinated water molecules (q values) at the metal center were 1.42 and 1.22, respectively, according to eq 1.[26] Thus, the lanthanide hydration state was hardly affected by the addition of Zn^{2+}. Therefore, it can be considered that the increase of the emission intensity caused by Zn^{2+} addition was not due to a change in the direct interaction of water molecules with Eu^{3+}.

no. of water molecules:

$$q^{Eu} = 1.2(\tau_{H_2O}{}^{-1} - \tau_{D_2O}{}^{-1} - 0.25) \quad (1)$$

Next, the spatial arrangement of **[Eu-7]** was further assessed by measuring the relaxometric properties. The water proton relaxivity R_1 of Gd^{3+} complexes is routinely used as an important parameter for MRI contrast agents.[27] The relaxation enhancement is modulated by the electron–nucleus dipolar interaction, which can be changed by rotation of the complex, by electron spin relaxation of the metal ion, and by the coordinated exchange of water molecules.[28] The R_1 relaxivity of **[Gd-7]** at 20 MHz showed similar values in the absence and in the presence of Zn^{2+}, i.e., 6.05 and 5.81 mM^{-1} s^{-1}, respectively. This result indicates that the environment around the Eu^{3+} ion of **[Eu-7]** was hardly changed by Zn^{2+} binding.

Effect of pH and Other Cations on the Long-Lived Luminescence Intensity. The luminescence emission intensity of **[Eu-7]** at 614 nm was examined at various pH values, with excitation at 320 nm. There was almost no effect of H^+ on the emission spectrum of **[Eu-7]** between pH 3.6 and 8.8 either in the presence or in the absence of Zn^{2+} (see Supporting Information). Thus, the luminescence emission intensity of **[Eu-7]** is stable at around physiological pH. Parker et al. reported a Zn^{2+}-sensitive luminescent lanthanide probe based on photo-induced electron transfer (PeT) from the benzylic nitrogen to the chromophore's singlet excited state.[19a,c] This approach has the disadvantage that the pivotal nitrogen for Zn^{2+} binding can also be protonated at lower pH, resulting in strong luminescence owing to inhibition of PeT. However, our compound **[Eu-7]** was not affected by lowering of the pH. The tertiary amine of **[Eu-7]** can be protonated at around pH 3.6, because TPA has pK_a values of 6.10, 4.28, and 2.49.[24] Thus, the finding of insensitivity to lower pH means that the luminescence augmentation was not due to cessation of PeT from tertiary amine. We think that this pH stability of the luminescence is one of the key advantages of **[Eu-7]**.

The effect of adding Na^+, K^+, Ca^{2+}, Mg^{2+}, and various heavy metal ions on the luminescence emission intensity of **[Eu-7]** was also examined. Luminescence emission enhancement of

(23) (a) Crosby, G. A.; Whan, R. E.; Alire, R. M. *J. Chem. Phys.* **1961**, *34*, 743–748. (b) Stein, G.; Würzberg, E. *J. Chem. Phys.* **1975**, *62*, 208–213.
(24) Martell, A. E.; Smith, R. M. *NIST Critically Selected Stability Constants of Metal Complexes*; NIST Standard Reference Database 46, Version 6.0; NIST: Gaithersburg, MD, 2001.
(25) (a) Weiss, J. H.; Sensi, S. L.; Koh, J. Y. *Trends Pharmacol. Sci.* **2000**, *21*, 395–401. (b) Li, Y.; Hough, C. J.; Suh, S. W.; Sarvey, J. M.; Frederickson, C. J. *J. Neurophysiol.* **2001**, *86*, 2597–2604. (c) Li, Y.; Hough, C. J.; Frederickson, C. J.; Sarvey, J. M. *J. Neurosci.* **2001**, *21*, 8015–8025.
(26) Beeby, A.; Clarkson, I. M.; Dickins, R. S.; Faulkner, S.; Parker, D.; Royle, L.; de Sousa, A. S.; Williams, J. A. G.; Woods, M. *J. Chem. Soc., Perkin Trans. 2* **1999**, 493–503.
(27) (a) Caravan, P.; Ellison, J. J.; McMurry, T. J.; Lauffer, R. B. *Chem. Rev.* **1999**, *99*, 2293–2352. (b) Lowe, M. P. *Aust. J. Chem.* **2002**, *55*, 551–556. (c) Li, W. H.; Fraser, S. E.; Meade, T. J. *J. Am. Chem. Soc.* **1999**, *121*, 1413–1414. (d) Li, W. H.; Parigi, G.; Fragai, M.; Luchinat, C.; Meade, T. J. *Inorg. Chem.* **2002**, *41*, 4018–4024. (e) Moats, R. A.; Fraser, S. E.; Meade, T. J. *Angew. Chem., Int. Ed. Engl.* **1997**, *36*, 726–728. (f) Louie, A. Y.; Hüber, M. M.; Ahrens, E. T.; Rothbächer, U.; Moats, R.; Jacobs, R. E.; Fraser, S. E.; Meade, T. J. *Nat. Biotechnol.* **2000**, *18*, 321–325.
(28) Merbach, A. E.; Tóth, É. *The Chemistry of Contrast Agents in Medical Magnetic Resonance Imaging*; John Wiley & Sons, Ltd.: Chichester, 2001.

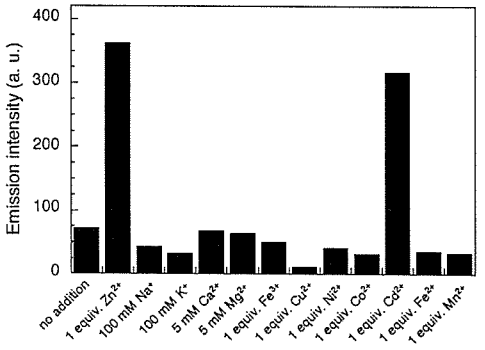

Figure 5. Luminescence intensity change profiles of **[Eu-7]** (50 μM) in the presence of various cations in 100 mM HEPES buffer at pH 7.4, 22 °C (excitation 320 nm, emission 614 nm). Heavy metal ions (1 equiv relative to **[Eu-7]**) were added as $Fe_2(SO_4)_3$, $CuSO_4$, $NiSO_4$, $CoSO_4$, $CdSO_4$, $FeSO_4$, and $MnSO_4$. Other cations were added as $ZnSO_4$ (50 μM), $NaNO_3$ (100 mM), KNO_3 (100 mM), $CaCl_2$ (5 mM), and $MgSO_4$ (5 mM).

[Eu-7] (50 μM) was not observed upon the addition of 100 mM Na^+ or K^+, 5 mM Ca^{2+} or Mg^{2+}, or 50 μM of various heavy metal ions except for Cd^{2+} (Figure 5). Thus, Na^+, K^+, Ca^{2+}, and Mg^{2+}, which exist at high concentrations in biological systems, did not enhance the luminescence intensity of **[Eu-7]**. The luminescence emission intensity was weakened or quenched upon the addition of several cations (particularly Cu^{2+}, Ni^{2+}, and Co^{2+}) together with Zn^{2+}, in comparison with that upon adding Zn^{2+} alone, as shown in Figure S8. However, Zn^{2+} can be distinguished from these heavy metals, since Zn^{2+} chelation selectively enhances the luminescence intensity.

Utility of the Long-Lived Luminescence. To explore further the utility of the long luminescence lifetime of **[Eu-7]**, we tested whether it could be well distinguished from the short-lived background fluorescence and scattered light. Figure 6 presents the emission spectra of **[Eu-7]** solution, with 1 μM rhodamine 6G as an artificial short-lived background, without (Figure 6a) or with (Figure 6b) a time resolution process. There are three fluorescent peaks in Figure 6a due to scattered light (300 nm), the increased fluorescence of the quinoline moiety (around 400 nm), and the fluorescence of rhodamine 6G (around 550 nm). Among them, rhodamine 6G fluorescence can directly interfere with Eu^{3+} luminescence. However, the long-lived luminescence detection of **[Eu-7]** solution was not affected at all by these three peaks (Figure 6b). Thus, the luminescence of **[Eu-7]** should be little influenced by experimental artifacts when measured with the aid of a time-resolution process.

Biological Applications of [Eu-7]. We next examined the application of **[Eu-7]** to cultured living cells (HeLa cells) by fluorescence microscopy (Figure 7). Since **[Eu-7]** can be excited with a relatively long excitation wavelength, this compound is suitable for cellular applications, in contrast to previously reported Zn^{2+}-sensitive luminescent lanthanide sensors. The fluorescence microscope had an optical window centered at 617 ± 37 nm for the emission due to Eu^{3+}-based luminescence upon excitation at 360 ± 40 nm (the Stoke's shift is >250 nm). Compound **[Eu-7]** was injected only into the single cultured HeLa cell in the bottom left-hand part of the field of view in Figure 7. We then added Zn^{2+} (150 μM) and a zinc-selective ionophore, pyrithione (2-mercaptopyridine *N*-oxide, 50 μM), to the medium at 3 min, inducing a prompt increase of intracellular luminescence. This luminescence was decreased by extracellular

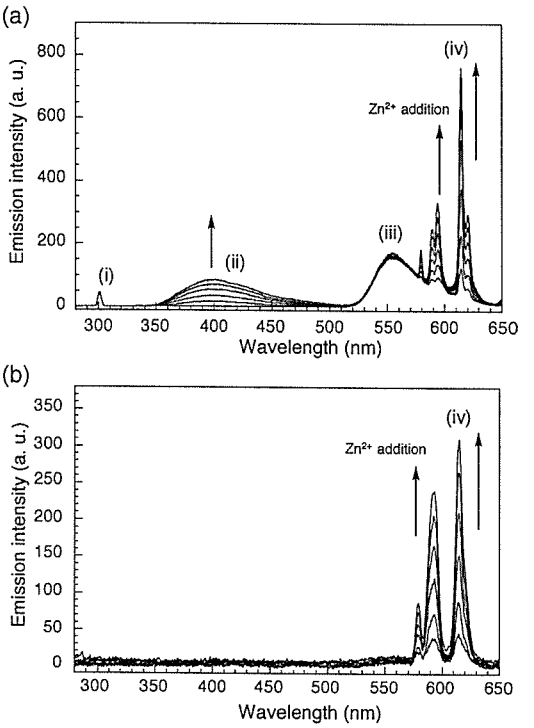

Figure 6. Emission spectra of **[Eu-7]** (50 μM) without (a) and with (b) time resolution in the presence of various concentrations of Zn^{2+}: 0, 0.2, 0.4, 0.6, 0.8, and 1.0 equiv of Zn^{2+} with respect to **[Eu-7]** (excitation at 300 nm, respectively). Both spectra were measured in 100 mM HEPES buffer containing 1 μM rhodamine 6G as a chromophore to provide artificial background fluorescence at pH 7.4 and 22 °C. The emission spectra (a) were measured with a Hitachi F4500, and the time-resolved emission spectra (b) were measured using a delay time of 0.05 ms and a gate time of 1.00 ms with a Perkin-Elmer LS-50B. Bands can be assigned to (i) scattered excitation light, (ii) the fluorescence of the quinolyl chromophore of **[Eu-7]**, (iii) the fluorescence of rhodamine 6G, and (iv) the long-lived luminescence of **[Eu-7]**.

addition of the cell-membrane-permeable chelator TPEN (150 μM) at 7.5 min. Clear images were obtained, because **[Eu-7]** has long-wavelength emission with a large Stoke's shift, which minimizes the influence of the excitation light. These results demonstrate that **[Eu-7]** can be used to monitor changes of intracellular ionic Zn^{2+} reversibly, and has potential for biological applications.

Conclusions

We have designed and synthesized a novel lanthanide-based luminescent sensor molecule for Zn^{2+}, **[Eu-7]**, by using Eu^{3+} as the fluorophore and a quinolyl moiety as the antenna. This compound **[Eu-7]** showed pronounced long-lived luminescence enhancement upon Zn^{2+} addition. Previously reported Zn^{2+}-sensitive lanthanide sensors are not suitable for biological applications, because of their short excitation wavelength, small enhancement of emission, inconvenient pH sensitivity, etc. In contrast, the properties with **[Eu-7]** are favorable for biological applications. It is noteworthy that **[Eu-7]** has a longer excitation wavelength than previously reported Zn^{2+}-sensitive lanthanide sensors, and this permits fluorescence microscopy measurements with **[Eu-7]** to monitor Zn^{2+} concentrations in living cells. We expect that a larger signal-to-noise ratio in cellular imaging

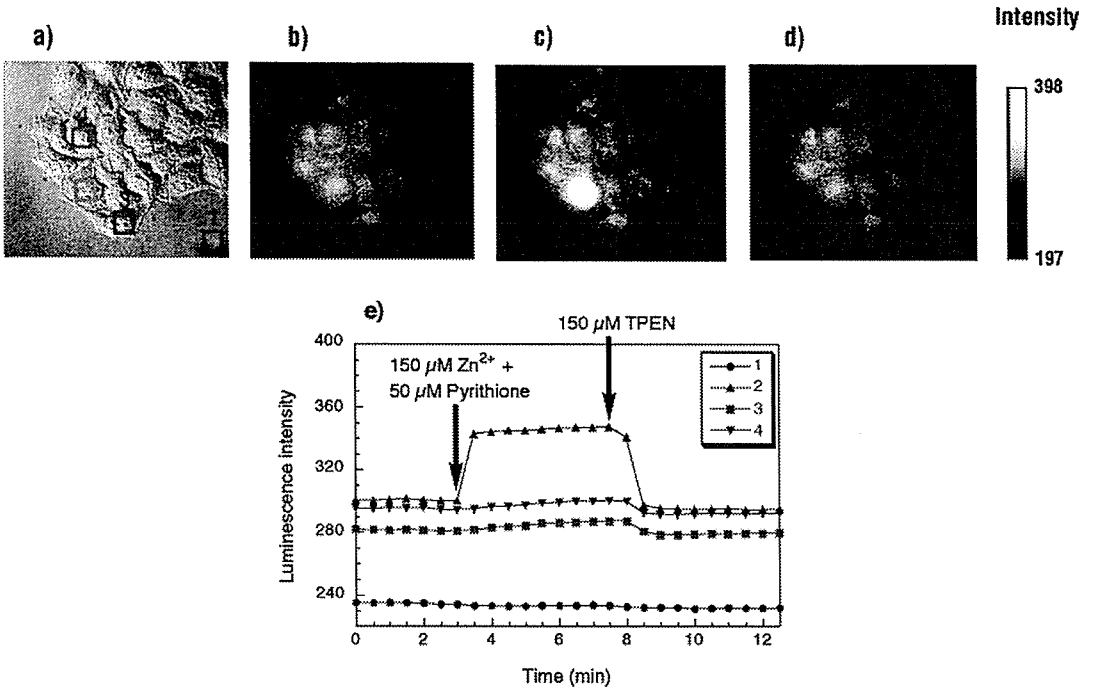

Figure 7. Bright-field transmission and luminescence images of Zn^{2+} in **[Eu-7]**-injected HeLa cells in HBSS buffer. The luminescence at 580−654 nm, excited at 320−400 nm, was measured at 30 s intervals. The cells were cultured in DMEM supplemented with 10% fetal bovine serum, 1% penicillin, and 1% streptomycin at 37 °C in a 5% CO_2/95% air incubator. The cells were then washed with HBSS buffer and injected with **[Eu-7]** solution. (a) Bright-field transmission image (0 min). (b) Luminescence image of (a) (0 min). (c) Luminescence image (5 min) following an addition of 50 μM pyrithione (zinc ionophore) and 150 μM $ZnSO_4$ to the medium at 3 min. (d) Luminescence image (10 min) following an addition of 150 μM TPEN to the medium at 7.5 min. Luminescence images (b−d) correspond to the luminescence intensity data in (e), which shows the average intensity of the corresponding area or cell area (1, extracellular region; 2, intracellular region of the injected cell; 3, 4, intracellular regions of noninjected cells).

would be achievable by using time-resolved imaging with **[Eu-7]**. Furthermore, we confirmed the advantage of the long-lived luminescence of **[Eu-7]** for eliminating fluorescence background interference. This complex **[Eu-7]** is the first Zn^{2+}-sensitive luminescent lanthanide chemosensor that can be used for studies on the biological functions of Zn^{2+}, and our design strategy should yield a range of long-lived luminescent lanthanide probes for sensing Zn^{2+} or, after appropriate modification of the acceptor moiety, other molecules of interest in biological applications.

Experimental Section

Materials. DTPA bisanhydride was purchased from Aldrich Chemical Co. Inc. (St. Louis, MO). All other reagents were purchased from either Tokyo Kasei Kogyo Co., Ltd. (Japan) or Wako Pure Chemical Industries, Ltd. (Japan). All solvents were used after distillation. Silica gel column chromatography was performed using BW-300, Chromatorex-NH, and Chromatorex-ODS (all from Fuji Silysia Chemical Ltd.).

Instruments. ^1H and ^{13}C NMR spectra were recorded on a JEOL JNM-LA300. Mass spectra were measured with a JEOL JMS-DX 300 mass spectrometer (EI^+) or a JEOL JMS-700 mass spectrometer (FAB^+). HPLC purification was performed on a reverse-phase column (GL Sciences (Tokyo, Japan), Inertsil Prep-ODS 30 mm × 250 mm) fitted on a Jasco PU-1587 System. Time-resolved fluorescence spectra were recorded on a Perkin-Elmer LS-50B (Beaconsfield, Buckinghamshire, England). The slit width was 5 nm for both excitation and emission. UV−visible spectra were obtained on a Shimadzu UV-1600 (Tokyo, Japan). Fluorescence spectroscopic studies were performed with a Hitachi F4500 (Tokyo, Japan). The slit width was 2.5 nm for both excitation and emission. The photomultiplier voltage was 700 V. Measurements of relaxation times T_1 were made using an NMR analyzer operating at 20 MHz (Minispec mq20, Bruker).

Time-Delayed Luminescence Spectral Measurements. The time-delayed luminescence spectra of **[Eu-7]** (50 μM) were measured in 100 mM HEPES buffer at pH 7.4, 22 °C (excitation at 320 nm), with addition of various amounts of Zn^{2+} (0, 0.1, 0.2, 0.3, 0.4, 0.5, 0.6, 0.7, 0.8, 0.9, 1.0, 1.1, 1.2, 2.0, 3.0, 4.0, 5.0, and 10.0 equiv of Zn^{2+}) to **[Eu-7]**. The slit width was 5 nm for both excitation and emission. A delay time of 0.05 ms and a gate time of 1.00 ms were used.

UV−Visible Absorption Spectral Measurements. The absorption spectral changes of **[Eu-7]** (50 μM) upon addition of Zn^{2+} were measured at 22 °C in an aqueous solution buffered to pH 7.4 (100 mM HEPES buffer). Zn^{2+} was added as $ZnSO_4$ at 0, 0.2, 0.4, 0.6, 0.8, 1.0, 2.0, 3.0, 4.0, 5.0, and 10.0 equiv of Zn^{2+} with respect to **[Eu-7]**.

Fluorescence Emission Spectral Measurements. The fluorescence emission spectra of **[Eu-7]** (20 μM) without a delay time were measured in 100 mM HEPES buffer (pH 7.4) at 22 °C, following excitation at 320 nm. The amounts of added Zn^{2+} were 0, 0.2, 0.4, 0.6, 0.8, 1.0, 2.0, 3.0, 4.0, 5.0, and 10.0 equiv with respect to **[Eu-7]**.

Quantum Yield Measurements. The luminescence spectra were measured with a Hitachi F4500 spectrofluorometer. The slit width was 2.5 nm for both excitation and emission. The photomultiplier voltage was 950 V. The luminescence spectra of **[Eu-7]** were measured in 100 mM HEPES buffer at pH 7.4, 25 °C, with irradiation at 300 nm. The quantum yields of Eu^{3+} complexes were evaluated using a relative method with reference to a luminescence standard, $[Ru(bpy)_3]Cl_2$ (ϕ = 0.028 in air-equilibrated water).[29] The quantum yields of Eu^{3+} complexes can be expressed by eq 2,[30] where Φ is the quantum yield (subscript "st" stands for the reference and "x" for the sample), A is

(29) Nakamura, K. *Bull. Chem. Soc. Jpn.* **1982**, *55*, 2697−2705.

$$\Phi_x/\Phi_{st} = [A_{st}/A_x]\,[n_x^2/n_{st}^2]\,[D_x/D_{st}] \quad (2)$$

the absorbance at the excitation wavelength, n is the refractive index, and D is the area (on an energy scale) of the luminescence spectra. The samples and the reference were excited at the same wavelength. The sample absorbance at the excitation wavelength was kept as low as possible to avoid fluorescence errors ($A_{exc} < 0.06$).

Luminescence Lifetime Measurements. The luminescence lifetimes of the complexes were recorded on a Perkin-Elmer LS-50B. The data were collected with 10-μs resolution in H_2O (100 mM HEPES buffer at pH 7.4) and D_2O (100 mM HEPES buffer at pD 7.4, based on the equation pD = pH + 0.40[31]), and fitted to a single-exponential curve obeying eq 3, where I_0 and I are the luminescence intensities at the

$$I = I_0 \exp(-t/\tau) \quad (3)$$

time $t = 0$ and time t, respectively, and τ is the luminescence emission lifetime. Lifetimes were obtained by monitoring the emission intensity at 614 nm (λ_{ex} = 320 nm).

Relaxation Time Measurements. The relaxation time, T_1, of aqueous solutions of the Gd^{3+} complex **[Gd-7]** was measured in 100 mM HEPES buffer (pH 7.4) at 20 MHz and 25 °C (Minispec mq20, Bruker). The value of T_1 was measured from 10 data points generated by using the standard inversion–recovery procedure. The relaxivity, R_1 ($mM^{-1}\ s^{-1}$), of **[Gd-7]** was determined from the slope of the plot of $1/T_1$ vs [**[Gd-7]**] (0, 0.4, 0.6, 0.8, and 1.0 mM). The buffered Gd^{3+} complex ([**Gd-7**]) solution was allowed to equilibrate for at least 10 min after addition of $ZnSO_4$ aqueous stock solution.

Apparent Dissociation Constant (K_d) Measurements. Upon addition of various concentrations of Zn^{2+}, the luminescence intensity and the absorbance of **[Eu-7]** linearly changed up to a 1:1 $[Zn^{2+}]$/[**[Eu-7]**] molar ratio, and the luminescence and absorption spectra remained at a plateau with further addition of Zn^{2+}. Furthermore, the Job's plot analysis revealed that maximum luminescence intensity was obtained at a 1:1 ratio. These data suggested that **[Eu-7]** should form a 1:1 complex with Zn^{2+}. So, the apparent dissociation constant, K_d, was determined from the luminescence intensity in 100 mM HEPES buffer (pH 7.4, I = 0.1 ($NaNO_3$)) at 22 °C (λ_{exc} = 320 nm). $[Zn^{2+}]$ was controlled by using 0–9 mM $ZnSO_4$/10 mM NTA (nitrilotriacetic acid) systems[19b,32] below 398 nM free Zn^{2+} and unbuffered Zn^{2+} above 200 μM free Zn^{2+}. The luminescence intensity data were fitted to eq 4, and K_d was calculated, where F is the luminescence intensity, F_{max}

$$F = F_0 + (F_{max} - F_0)\,([Zn^{2+}]_f)/(K_d + [Zn^{2+}]_f) \quad (4)$$

is the maximum luminescence intensity, F_0 is the luminescence intensity with no addition of Zn^{2+}, and $[Zn^{2+}]_f$ is the free Zn^{2+} concentration. The value of K_d was determined from the fittings for the luminescence intensity data shown in the Supporting Information.

Phosphorescence Spectral Measurements. Phosphorescence spectra were obtained with a Hitachi F4500. The phosphorescence spectra of **[Gd-7]** (20 μM) in the absence and in the presence of Zn^{2+} (1 equiv relative to **[Gd-7]**) were measured at 77 K in MeOH:EtOH = 1:1 (excitation at 320 nm) (see Supporting Information). The slit width was 10.0 nm for excitation and 20.0 nm for emission. The photomultiplier voltage was 950 V.

Effect of pH on the Luminescence Intensity. The following buffers were used: 100 mM $ClCH_2COOH$–$ClCH_2COONa$ buffer (pH 3.6), 100 mM AcOH–AcONa buffer (pH 4.0–5.5), 100 mM morpholinoethanesulfonic acid (MES) buffer (pH 5.5–6.5), 100 mM HEPES buffer (pH 7.0–8.0), and 100 mM *N*-cyclohexyl-2-aminoethanesulfonic acid (CHES) buffer (pH 8.5–9.0). The luminescence intensity (excitation 320 nm, emission 614 nm) of each sample of **[Eu-7]** (50 μM) was plotted.

Metal Ion Selectivity Measurements. The luminescence emission enhancement of **[Eu-7]** was measured in 100 mM HEPES buffer (pH 7.4) at 22 °C (excitation 320 nm, emission 614 nm). Heavy metal ions (50 μM) were added as $Fe_2(SO_4)_3$, $CuSO_4$, $NiSO_4$, $CoSO_4$, $CdSO_4$, $FeSO_4$, and $MnSO_4$. Other cations were added as $ZnSO_4$ (50 μM), $NaNO_3$ (100 mM), KNO_3 (100 mM), $CaCl_2$ (5 mM), and $MgSO_4$ (5 mM).

Confirmation of the Utility of the Long Luminescence Lifetime of [Eu-7]. The emission spectra without a time-resolution process were measured with a Hitachi F4500. The time-resolved emission spectra were measured with a Perkin-Elmer LS-50B using a delay time of 0.05 ms and a gate time of 1.00 ms. Spectra of **[Eu-7]** (50 μM) with various concentrations of Zn^{2+} were measured in 100 mM HEPES buffer (pH 7.4) at 22 °C containing 1 μM rhodamine 6G as an artificial provider of short-lived background fluorescence (excitation at 300 nm). The amounts of added Zn^{2+} were 0, 0.2, 0.4, 0.6, 0.8, and 1.0 equiv of Zn^{2+} with respect to **[Eu-7]**.

Preparation of Cells. HeLa cells were cultured in Dulbecco's modified Eagle's medium (DMEM) (Invitrogen Corp., Carlsbad, CA), supplemented with 10% fetal bovine serum (Invitrogen Corp.), 1% penicillin, and 1% streptomycin (Invitrogen Corp.) at 37 °C in a 5% CO_2/95% air incubator. The cells were grown on an uncoated 35-mm-diameter glass-bottomed dish (MatTek, Ashland, MA), and washed twice with Hanks' balanced salt solution (HBSS) buffer (Invitrogen Corp.), and then the medium was replaced with HBSS buffer before imaging. The compound **[Eu-7]** (2 mM) was dissolved in microinjection buffer (HBSS buffer), and injected into the cells with an Eppendorf injection system (Transjector 5246).

Microscopy and Imaging Methods. The imaging system comprised an inverted microscope (IX71; Olympus) and a cooled CCD camera (Cool Snap HQ; Roper Scientific, Tucson, AZ). The microscope was equipped with a xenon lamp (AH2-RX; Olympus), a 40× objective lens (Uapo/340, N.A. 1.35; Olympus), a dichroic mirror (420DCLP; OMEGA), an excitation filter (S360/40×; Chroma), and an emission filter (S617/73m; Chroma). The whole system was controlled using MetaFluor 6.1 software (Universal Imaging, Media, PA). The luminescence images were measured every 30 s. Additions of zinc sulfate (150 μM) with pyrithione (50 μM) or *N,N,N',N'*-tetra(2-picolyl)-ethylenediamine (TPEN) (150 μM) to cell samples were performed on the microscope stage.

Acknowledgment. This work was supported in part by the Ministry of Education, Culture, Sports, Science and Technology of Japan (Grants for The Advanced and Innovational Research Program in Life Sciences to T.N., 15681012 and 16048206 to K.K.). K.K. was also supported by the Sankyo Foundation, by the Kanagawa Academy of Science, and by the Suzuken Memorial Foundation. K.H. is the recipient of Research Fellowships of the Japan Society for the Promotion of Science for Young Scientists.

Supporting Information Available: Detailed descriptions of synthetic procedures for **[Eu-7]** and **[Gd-7]**; data on the measurements of the emission lifetime of **[Eu-7]** and on the measurement of the apparent dissociation constant of **[Eu-7]** with Zn^{2+}; phosphorescence spectra of **[Eu-7]**; plot of the absorbance intensity changes detected at 340 nm, shown in Figure 3; Job's plot for complexation between **[Eu-7]** and Zn^{2+}; plot of the changes in the fluorescence intensity detected at 397 and 614 nm, shown in Figure 4; and pH profile of the luminescence intensity of **[Eu-7]**. This material is available free of charge via the Internet at http://pubs.acs.org.

JA0469333

(30) Chen, Q. Y.; Feng, C. J.; Luo, Q. H.; Duan, C. Y.; Yu, X. S.; Liu, D. J. *Eur. J. Inorg. Chem.* **2001**, 1063–1069.
(31) Wang, Y. M.; Wang, Y. J.; Wu, Y. L. *Polyhedron* **1998**, *18*, 109–117.
(32) Hirano, T.; Kikuchi, K.; Urano, Y.; Higuchi, T.; Nagano, T. *J. Am. Chem. Soc.* **2000**, *122*, 12399–12400.

J|A|C|S
ARTICLES
Published on Web 06/15/2004

Nonspecific Medium Effects versus Specific Group Positioning in the Antibody and Albumin Catalysis of the Base-Promoted Ring-Opening Reactions of Benzisoxazoles

Yunfeng Hu,[†] K. N. Houk,*[,†] Kazuya Kikuchi,[‡] Kinya Hotta,[‡] and Donald Hilvert*[,‡]

Contribution from the Department of Chemistry and Biochemistry, University of California, Los Angeles, Los Angeles, California 90095-1569 and Department of Chemistry, Scripps Research Institute, La Jolla, California 92037, and Laboratorium für Organische Chemie, Swiss Federal Institute of Technology, ETH−Hönggerberg, CH-8093, Zürich, Switzerland

Received February 18, 2004; E-mail: houk@chem.ucla.edu; hilvert@org.chem.ethz.ch

Abstract: The mechanisms by which solvents, antibodies, and albumins influence the rates of base-catalyzed reactions of benzisoxazoles have been explored theoretically. New experimental data on substituent effects and rates of reactions in several solvents, in an antibody, and in an albumin are reported. Quantum mechanical calculations were carried out for the reactions in water and acetonitrile, and docking of the transition state into a homology model of antibody 34E4 and an X-ray structure of human serum albumin was accomplished. A microenvironment made up of catalytic polar groups (glutamate in antibody 34E4 and lysine in human serum albumin) surrounded by relatively nonpolar groups is present in both catalytic proteins.

Introduction

The conversions of benzisoxazoles to cyanophenoxides with bases and various catalysts, often referred as the "Kemp elimination,"[1a−b] have been used as a probe of medium effects on the rates of reactions (Figure 1). The rates of these reactions are very sensitive to solvent polarity. Kemp and co-workers' classic studies of the effect of substituents and solvents established that the acetate-promoted reaction of 5-nitrobenzisoxazole is 10^8 times faster in acetonitrile than water.[1c−d] This reaction has subsequently been shown to be catalyzed by catalytic antibodies ($k_{cat}/k_{uncat} = 10^6$),[2] serum albumins (10^3),[3−5] orphan antibodies (10^3),[6] a polyamine organic host (10^3),[7] surfactant vesicles (850),[8] micelles (400),[8] polyethyleneimine "synzymes" (10^5 per site),[9] and even coal (200).[10] Because

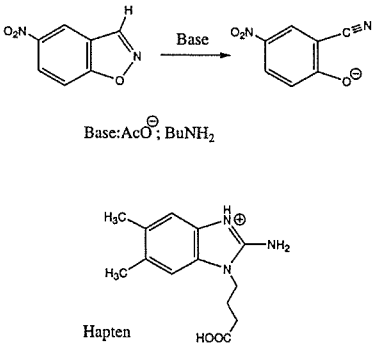

Figure 1. Base-catalyzed decomposition of benzisoxazoles (the "Kemp elimination") and the hapten used to elicit antibody 34E4.

different authors use different definitions for k_{cat} and k_{uncat}, those accelerations are not always directly comparable. For example, k_{uncat} can be considered as a pseudo-first-order rate constant of a water catalyzed reaction, or a second-order rate constant of an acetate or amine base-promoted reaction in water, whereas k_{cat} can be either a second-order rate constant in base-promoted reactions in different solvents or a first-order rate constant when saturated protein catalysts are involved. The various rate constants in different catalytic systems and the k_{uncat} used to compute them are listed in Table 1. The magnitude of the rate acceleration clearly depends on the pK_a of the base responsible for deprotonation and hence on the pH of the reaction medium. Catalysts such as antibody 34E4 and the polyethyleneimine "synzymes" exhibit high rate accelerations at pH values near their pK_a (ca. 6), whereas catalysts such as BSA with higher pK_a's (ca. 10) must contend with the high background rate at

[†] University of California, Los Angeles.
[‡] Scripps Rsearch Institute and Swiss Federal Institute of Technology.

(1) (a) Casey, M. L.; Kemp, D. S.; Paul, K. G.; Cox, D. D. *J. Org. Chem.* **1973**, *38*, 2294−2301. (b) Kemp, D. S.; Casey, M. L. *J. Am. Chem. Soc.* **1973**, *95*, 6670−6680. (c) Kemp, D. S.; Paul, K. *J. Am. Chem. Soc.* **1975**, *97*, 7305−7312. (d) Kemp, D. S.; Cox, D. D.; Paul, K. *J. Am. Chem. Soc.* **1975**, *97*, 7312−7318.
(2) Thorn, S. N.; Daniels, R. G.; Auditor, M.-T. M.; Hilvert, D. *Nature* **1995**, *373*, 228−230.
(3) Hollfelder, F.; Kirby, A. J.; Tawfik, D. S. *Nature* **1996**, *383*, 60−63.
(4) Kikuchi, K.; Thorn, S. N.; Hilvert, D *J. Am. Chem. Soc.* **1996**, *118*, 8184−8185.
(5) Hollfelder, F.; Kirby, A. J.; Tawfik, D. S.; Kikuchi, K.; Hilvert, D. *J. Am. Chem. Soc.* **2000**, *122*, 1022−1029.
(6) Genre-Grandpierre, A.; Tellier, C.; Loirat, M. J.; Blanchard, D.; Hodgson, D. R. W.; Hollfelder, F.; Kirby, A. J. *Bioorg. Med. Chem. Lett.* **1997**, *7*, 2497−2502.
(7) Kennan, A. J.; Whitlock, H. W. *J. Am. Chem. Soc.* **1996**, *118*, 3027−3028.
(8) Perez-Juste, J.; Hollfelder, F.; Kirby, A. J.; Engberts, J. B. F. N. *Org. Lett.* **2000**, *2*, 127−130.
(9) Hollfelder, F.; Kirby, A. J.; Tawfik, D. S. *J. Org. Chem.* **2001**, *66*, 5866−5874.
(10) Shulman, H.; Keinan, E. *Org. Lett.* **2000**, *2*, 3747−3750.

10.1021/ja0490727 CCC: $27.50

Table 1. Rate Constants for the Uncatalyzed and Catalyzed Decarboxylations of 5-Nitrobenzisoxazoles in Different Catalytic Systems

catalyst	$k_{background}$ (s^{-1})[j]	k_{cat} (s^{-1})
34E4[a]	3.1×10^{-5}	0.66
34E4[b]	2.2×10^{-7}	0.30
BSA[c]	1.6×10^{-3}	2.5
BSA[d]	3.1×10^{-5}	0.017
orphan antibody 4B2[e]	$>3.1 \times 10^{-5}$	0.035
organic host[f]	1.1×10^{-7}	0.00063
coal[g]	6.8×10^{-5}	0.014
synzyme[h]	8.0×10^{-8}	0.045
Bu_4NOAc[i]	1.4×10^{-4} M^{-1}	
Et_3N[i]	8.2×10^{-1} M^{-1}	

[a] 20 °C, 40 mM phosphate buffer containing 100 mM NaCl, pH 7.4, ref 2. [b] 20 °C, 40 mM sodium acetate buffer containing 100 mM NaCl, pH 6.0 (the pK_a of the active site carboxylic acid), ref 2 and this work. [c] 20 °C, 40 mM sodium carbonate buffer containing 100mM NaCl, pH 10.2 (the pK_a of the active site amine), ref 4 and this work. [d] 20 °C, 40 mM phosphate buffer containing 100 mM NaCl, pH 7.4, Reference 4. [e] 30 °C, 1% CH_3CN, 40 mM phosphate buffer containing 100 mM NaCl, pH 7.1, ref 6. The value of $k_{background}$ originally reported in ref 6 is 1.9×10^{-6} s^{-1}, which is inconsistently low and is presumably a misprint. [f] Room temperature, $CDCl_3$, ref 7. [g] 4 °C, 50 mM phosphate buffer containing 2% acetonitrile, pH 7.4, ref 10. [h] 25 °C, 70 mM BisTris buffer, pH 5.9, ref 9. [i] 25° C, H_2O, ref 1d. [j] $k_{background}$ is obtained by extrapolation to zero buffer concentration.

high pH and are less efficient even though the absolute value of k_{cat} in the pH-independent range is higher.

Although many different interpretations have been offered for the catalysis by these diverse materials, the binding of substrate into a relatively nonpolar environment and particularly the desolvation of acetate have usually been thought to be responsible for the rate acceleration. By contrast, the amine-catalyzed reaction is relatively insensitive to solvent polarity, presumably because the uncharged base is not dramatically stabilized by hydrogen bonding. Thus, the reactions involving amine bases, such as polyamines, serum albumins, and synzymes are not easy to explain by medium polarity effects.

Vigorous discussion has broken out about how two types of protein catalysts, (1) tailored catalytic antibodies such as 34E4,[2] and (2) "off-the-shelf" proteins such as serum albumins,[3,4] accelerate this transformation. The two proteins are likely to exploit carboxylate and amine groups as catalytic bases, respectively. Hilvert and Kirby independently determined that serum albumins catalyze the Kemp ring-opening with k_{cat} similar to that found with catalytic antibody 34E4.[3,4] Hilvert identified Lys222 as the catalytic group in bovine serum albumin subdomain II A. There is also a set of positively charged residues that stabilize the phenolate product formed in the reaction.[4] However, Kirby proposed that the low polarity of the interiors of the albumin and 34E4 is the factor responsible for most of the rate acceleration in both cases.[3]

We have studied how these different proteins accelerate this reaction. Kinetic measurements on substituted compounds have been performed to show how specific interactions with nonpolar residues and nonspecific medium effects influence the stability and structure of the transition state. Quantum mechanical calculations of acetate and amine catalyzed reactions in the gas phase and in nonpolar and aqueous solutions have been used to explore the origins of acceleration by nonpolar solvents. The docking and binding of reactants and transition states in the antibody and serum albumin have provided detailed pictures of the origins of antibody and protein catalysis, specifically relative importance to catalysis of polarity and positioning of functional groups in the binding site.

Whether or not proteins can accelerate reactions merely by altering the microenvironment around a substrate and transition state has been the subject of an ongoing debate. Dewar attributed catalysis of chymotrypsin and carboxypeptidase A to the ability of these enzymes to eliminate solvent from the binding pocket and to provide a nonpolar environment for the reaction.[11] He also emphasized the importance of a nonpolar environment for acceleration of various reaction types.[12] On the other hand, Warshel has used thermodynamic arguments to show that desolvation effects alone are unlikely to be the origin of enzyme activity.[13] Although a polar molecule is destabilized by being bound into a nonpolar environment, a free energy penalty must be paid to remove the ionic molecule from water. Warshel proposes that electrostatic interactions between the oriented dipoles of the preorganized protein binding pocket and the substrate generally cause catalysis.[13] In general, Warshel embraces the effectively high polarity of protein binding sites and attributes catalysis to the ideal electrostatic complementarity of protein binding site and transition state.

Although some investigators have advocated pure medium effects ("The medium is the message" in McLuhan's words),[3] others have highlighted contributions of structural effects and specific interactions to catalysis. For example, Bruice emphasizes the ability of a protein to assemble substrates specifically into a geometry suitable for reaction (NACs, near attack conformations) regardless of the polarity of the microenvironment.[14]

Throughout these discussions, confusion has occasionally arisen by the use of different definitions of "medium." The dictionary definition emphasizes more or less homogeneous surroundings: "Any intervening substance through which a force acts on objects at a distance or through which impressions are conveyed to the senses: applied, e.g., to the air, the ether, or any substance considered with regard to its properties as a vehicle of light or sound."[15] This definition of "medium" implies a homogeneous environment. However, the word is often used to indicate specific characteristics of surroundings even when they are heterogeneous. "Microenvironment" is used here as a term to describe the active site of a protein catalyst, especially to convey the heterogeneity that is always a characteristic of a protein interior.

Kinetic Studies. Kemp explored the kinetics of the reactions of substituted benzisoxazoles (BI) with tertiary amines in water.[1] The kinetics follow Brønsted linear free energy relationships (LFERs) over a broad range of reactivity. The slope, β, of a plot of log k vs pK_a of the leaving group, pK_{lg}, provides a measurement of the relationship between the reaction rate and the reaction exothermicity and yields information about the structure and solvation of the transition state (TS).[16] We have measured the rates and β_{lg} values for these eliminations in several solvents and with protein catalysts. These are compared to water as a standard. Table 2 lists the benzisoxazoles studied,

(11) Dewar, M. J. S.; Storch, D. M. *Proc. Natl. Acad. Sci. U.S.A.* **1985**, *82*, 2225–2229.
(12) Dewar, M. J. S.; Healy, E. *Organometallics* **1982**, *1*, 1705–1708.
(13) Warshel, A. *J. Biol. Chem.* **1998**, *273*, 27035–29038.
(14) Bruice, T. C.; Lightstone, F. C. *Acc. Chem. Res.* **1999**, *32*, 127–136.
(15) Oxford English Dictionary, Second Edition, 1989.
(16) Hammond, G. S. *J. Am. Chem. Soc.* **1955**, *77*, 334–338; Leffler, J. E. *Science* **1953**, *117*, 340–341.